

Dislocation and disclination densities in experimentally deformed polycrystalline olivine

Pre-print, non-peer reviewed, submitted to European Journal of Mineralogy in sept 2022

5 Sylvie Demouchy^{1,2,*}, Manuel Thieme¹, Fabrice Barou¹, Benoit. Beausir^{3,4}, Vincent Taupin^{3,4}, Patrick Cordier^{5,6}

¹ Geosciences Montpellier, Université de Montpellier & CNRS, UMR 5243, F-34095 Montpellier, France

² Laboratoire Magmas et Volcans, Université Clermont Auvergne, CNRS, IRD & OPGC, UMR 6524, F-63170 Aubière, France.

³ Université de Lorraine, CNRS, LEM3, F-57000 Metz, France

10 ⁴ Laboratory of Excellence Design of Alloy Metals for low-mAss Structures (DAMAS), University of Lorraine, F-57073 Metz, France

⁵ Univ. Lille, CNRS, INRAE, Centrale Lille, UMR 8207 - UMET - Unité Matériaux et Transformations, F-59000 Lille, France

⁶ Institut Universitaire de France, F-75005 Paris, France

15 *Correspondence to:* S.Demouchy (sylvie.demouchy@uca.fr)

Abstract. We report a comprehensive dataset characterizing and quantifying the dislocation density in the crystallographic frame (ρ_{α}^c) and disclination density (ρ_{θ}) in fine-grained polycrystalline olivine deformed in uniaxial compression or torsion, at 1000 °C and 1200 °C, under a confining pressure of 300 MPa. Finite strains range from 0.11 up to 8.6 % and stresses reach up to 1073 MPa. The data set is a selection of 19 electron backscatter diffraction maps acquired with conventional angular resolution (0.5°), but at high spatial resolution (step size from 0.05 to 0.1 μm). Thanks to analytical improvement for data acquisition and treatment with notably the use ATEX software, we report spatial distribution of both geometrically necessary dislocation (GND) and disclination densities. Area with the highest GND densities define subgrain boundaries. The type of GND densities involved also indicate that most olivine subgrain boundaries have mixed character. Moreover, strategy for visualization also permit to identify a population of minor GND, not well organized. Low temperature and high stress sample displays a higher, but less organized GND density than sample deformed at high temperature for similar finite strain and identical strain rate, confirming the action of dislocation creep in these samples, even for small grain (2 μm). Furthermore, disclination dipoles along grain boundaries are identified in every undeformed and deformed EBSD maps, mostly at the triple junction of a grain boundary with a subgrain, but also along sub-grain boundaries, and at subgrain boundary tips. Nevertheless, for the range of parameters investigated, there is no notable correlation of the disclination density with stress, strain, or temperature. However, a positive correlation between average disclination density and average GND density per grain is found confirming their similar role as defects producing intragranular misorientation. Furthermore, a negative correlation between the disclination density and the grain size or perimeter is found, providing a first rule of thumb on the distribution of disclinations. Field Disclination and Dislocation Mechanics simulations of the elastic fields due

to experimentally measured dislocations and disclinations (e.g. strains/rotations and stresses), provide further evidence of the
35 interplay between both types of defects. At last, our results also support that disclinations act as a plastic deformation
mechanism, by allowing rotation of a very small crystal volume.

1 Introduction

As the most abundant (> 60 % in volume) and weakest mineral phase in the Earth's upper mantle, olivine dictates the upper
mantle rheology and hence the kinematics of the upper mantle convection and the relative rigidity of the overlying
40 lithospheric plate compared to the asthenosphere below. Experimental deformation of olivine at temperatures relevant to the
lithospheric mantle and subducting slabs (< 1200 °C) and extensive studies of mantle-derived xenoliths of peridotites show
that dislocation creep is the major deformation mechanism in the uppermost mantle (e.g., Hirth and Kohlstedt, 2003;
Tommasi and Vauchez, 2015; Bernard et al., 2019). This mechanism of deformation is rate-controlled by dislocations
motion, which are topological defects in the crystal lattice arising from translational lattice incompatibility (as measured by
45 the Burgers vector, b). Dislocations can exhibit conservative motion (glide) in some specific planes, defining slip systems
(slip direction and associated plane of glide). For a polycrystalline aggregate to undergo an arbitrary imposed homogenous
deformation, five independent slip systems are required (von Mises criterion, Mises, 1928; Hutchinson, 1977). Yet,
dislocations in olivine can only glide according to three independent slip systems ($[100](010)$, $[100](001)$, $[001](010)$ or
 $[100](010)$, $[001](010)$, $[001](100)$), which are directly constrained by the lack of glide in the $[010]$ direction (for a brief
50 review see Demouchy, 2021). Therefore, an additional degree of freedom must be provided, e.g. dislocation climb or grain
boundary mechanisms like grain boundary sliding or grain boundary migration. Nevertheless, (1) at temperatures < 1100 °C,
ionic diffusion and thus dislocation climb in olivine is a mechanism too slow to significantly contribute to macroscopic creep
(e.g. Goetze, 1978; Evans & Goetze, 1979; Hirth & Kohlstedt, 2003; Cordier et al., 2014), and (2) dislocation-
accommodated grain boundary sliding requires displacement and/or significant discontinuities at grain boundaries, including
55 cavitation (e.g., Langdon, 2006; Gasc et al., 2019). A novel solution was proposed as a complementary mechanism for creep
in olivine aggregates: Disclinations. Disclinations are rotational topological defects arising from rotational lattice
incompatibility (as expressed by the Frank rotational vector ω ; de Wit, 1970), which have been mostly reported in liquid
crystals (Voltera, 1907; Friedel, 1922; Frank, 1958). They were observed in polycrystalline metals (Beausir and Fressengeas,
2013; Fressengeas and Beausir, 2018), and in experimentally deformed polycrystalline olivine, but also in natural olivine-
60 rich rocks (Cordier et al., 2014) and where successfully modeled in forsterite (Sun et al., 2016, 2018). Historically,
disclinations were thought to be too high energetically to exist in crystalline solids such as silicates (Friedel, 1922; Hirth and
Lothe, 1982, p.4). In polycrystalline solids, disclinations are thought to arrange in self-screened configurations like dipoles,
thus significantly reducing the stored elastic energy in the deformed lattice (Romanov & Vladimirov, 1992; Romanov &
Kolesnikova, 2009; Cordier, 2014). As such, they can be used to describe the lattice structure when a single-valued elastic
65 rotation field does not exist, such as for grain boundaries (Li, 1972). Disclinations might therefore prove useful in modeling

high-angle grain boundaries, grain boundary ledges, deformation of nano-aggregates and grain boundaries as sources and sinks for dislocations (e.g., Kleman & Friedel, 2008). In forsterite, Heinemann et al. (2005) has shown that only grain boundaries with disorientation angles lower than 20 ° can be modeled with the classic dislocation-based Read-Shockley model (Read and Shockley, 1950). For high-angle boundaries, dislocation cores would overlap, invalidating this description. 70 Consequently, a solution is to introduce periodic arrays of disclination dipoles in high-angle grain boundaries models, which was achieved successfully in the recent years (e.g., Fressengeas et al., 2011; Upadhyay et al., 2011; Taupin et al., 2014; Sun et al., 2016, 2018). Further limitations in dislocation-based grain boundary models are induced by spatial considerations, which complicates three-dimensional grain networks models (Sutton & Vitek, 1983). Disclination-based models can overcome these limitations by implementing the discontinuities of the elastic displacement (i.e., relative rotation) of the 75 crystal lattice along grain boundaries.

In this paper we investigate the polycrystalline olivine microstructure at high spatial resolution using conventional electron backscatter diffraction (EBSD). Specifically, we quantify the geometrically necessary dislocation and disclination density in deformed polycrystalline olivine for a range of temperatures, finite strains and stresses. We use experimentally deformed samples at high pressure from previous studies (Demouchy et al. 2012 ; Thieme et al., 2018), providing a new dataset for 80 finite strains up to early steady state and temperatures of 1000 °C and 1200 °C. Additionally, we investigate the effect of acquisition setup (e.g., sample preparation and step size), data treatments such as range of disorientation, and display features such as smoothing and user-defined scale to define the best visual comfort for maps of disclination density.

2 Material & Methods

2.1 Experimental sample and preparation

85 We have selected experimentally seven deformed samples by Thieme et al. (2018) and one undeformed sample from Demouchy et al. (2012), see Table 1. All samples are synthesized from inclusion-free single crystals of San Carlos olivine washed and pulverized in a fluid energy mill, resulting in a grain equivalent diameter before hot-pressing and deformation of ~ 2 µm. San Carlos olivines have a mean composition of $(\text{Mg}_{0.91}\text{Fe}_{0.09}\text{Ni}_{0.003})_2\text{SiO}_4$ (e.g., Buening and Buseck, 1973; Frey and Prinz, 1978; Demouchy, 2010) and a naturally low water content (< 1 ppm wt H₂O, see e.g., Demouchy, 2010). 90 Orthopyroxene and chromite are expected as trace fraction only and their presence helped buffering the silica activity and oxygen fugacity, respectively.

The fine-grained powder of San Carlos olivine was first cold-pressed in Ni capsules, and subsequently sintered at 1200 °C and 300 MPa (Argon) for 3 h, producing dense polycrystalline cylinder ~8 mm in diameter and ~16 mm long. Sintered polycrystals were subsequently deformed in either uniaxial compression (Thieme et al., 2018) or torsion (Demouchy et al., 95 2012) in a high-pressure high-temperature deformation gas-medium apparatus (Paterson, 1990; Paterson and Olgaard, 2000). Confining pressure is 300 MPa for both type of experiments, temperature was set at 1000 °C or 1200 °C and equivalent strains range from 0.11 to 8.6 %. One sample (CMT16-7) is a sintered but undeformed aggregated used here as has a

reference ‘starting material’. Torsion sample PI0546 contains 45 μl of deionized water added to the cold-pressed aggregate, but very limited amount of hydrogen was embedded in the olivine lattice (see Demouchy et al., 2012 for details). The samples were previously examined by transmission electron microscopy and did not reveal the presence of cavitation induced by grain boundary sliding or stressed-induced amorphization of olivine inside the grain boundaries (Demouchy et al., 2012; Thieme et al., 2018; Samae et al., 2021). For the samples deformed in torsion, a section through the center of the sample and perpendicular to the shear direction was cut with a slow speed saw and embedded in epoxy, while samples were cut parallel to the deformation axis for the sample deformed in axial compression. Recovered samples were then polished, including a final chemo-mechanical polish using colloidal silica (0.04 μm particles, average polishing times of 1 h) for investigation in scanning electron microscopy (SEM) and electron backscatter diffraction (EBSD).

EBSD maps were acquired at the center of the sample deformed in axial compression, while for samples deformed in torsion, EBSD maps were acquired from three positions: (1) at the inner radius, that is at 2 mm from the outer edge (i.e.); (2) at the center of the sample, that is at 1 mm from the outer edge, and (3) at outer edge. Therefore, for the torsion sample there are three areas of investigation, corresponding to three different finite shear strains and shear strain rates. Three maps were acquired in each area (with different map sizes and acquisition set up). The shear strain γ was calculated as $\gamma = (\theta D/2l)$, where θ is the angular displacement, D the sample diameter and l the sample length. To allow comparison with samples deformed in uniaxial compression, the equivalent strain rate $\dot{\epsilon}$ was calculated as $\dot{\epsilon} = \dot{\gamma}/\sqrt{3}$, where $\dot{\gamma}$ is the shear strain rate. Likewise, the equivalent stress σ was calculated as $\sigma = \tau\sqrt{3}$, where τ is the shear stress (see Paterson and Olgaard, 2000; Demouchy et al., 2012).

2.2 Crystallographic orientation measurements and treatments

2.2.1 Acquisition

Olivine crystallographic orientation was obtained by EBSD with the CamScan X500FE CrystalProbe at Geosciences Montpellier (University of Montpellier, France). Exposed sample surfaces were partially coated with 2-5 nm of carbon, leaving a central uncoated window for EBSD mapping. The typical 1-inch epoxy plug was subsequently surrounded and partially covered by copper-carbon tape to improve conductivity and electron discharging in the sample chamber. This is a requirement for achieving high spatial resolution mapping on semi-conductive material such as fine-grained silicates. The beam acceleration voltage was 17-17.5 kV, beam current 10 nA and working distance 24-25.1 mm. We used a binning of 4 \times 4 for the EBSD camera (1/16 of the original resolution of the CCD camera) avoid charging effect for acquisition with a fine step size (<0.2 μm). Olivine, diopside, enstatite and Cr-spinel were acquired during mapping. EBSD data were recorded and cleaned using the HKL Aztec and Channel 5 softwares and further treated with ATEX software (Beausir and Fundenberger, 2017) to determine dislocation and disclination densities. The theoretical framework for disclinations detection and quantification is already fully detailed in Beausir and Fressengeas (2013), Cordier et al., (2014) and Fressengeas and Beausir, (2018) and will not be reproduced in full here, only the basic principles is recalled below.

130 The noise reduction of raw data is partially performed using Channel 5-Tango (Oxford Instruments HKL) software and finalized using ATEX software (Beausir and Fundenberger, 2017) and can also be done using MTEX (Matlab tool box, see Hielscher & Schaeben, 2008; Bachmann et al., 2010). The treatment consists of (1) removing the wild spikes defined as pixels with a misorientation of $> 1^\circ$ to at least seven neighbors ; (2) isolated non-indexed pixel and clusters of up to three non-indexed pixels are nullified, (3) orientations are filtered with a Kuwahara filter with two iterations and a maximum angle of 5° . This non-linear smoothing filter permit adaptive noise reduction and helps identifying subgrain boundary domains ; (4) internal disorientations $> 10^\circ$ define grain boundaries (displayed in dark green) (NB: 10° was chosen for consistency with Demouchy et al., 2012 and Thieme et al., 2018, while a value of 15° is usually chosen for data acquired on natural peridotites displaying millimetric grain size, e.g., Demouchy et al., 2019), and (5) disorientations between 1 and 10° define subgrain boundaries (displayed as pale grey lines). Finally, the densities of geometrically necessary dislocations, and the densities of disclinations are solely calculated along the olivine-olivine boundaries. Potential residual enstatites or Cr-spinel grains are excluded of the data treatment.

2.2.2 Geometrically necessary dislocation densities

The density of geometrically necessary dislocations (GND) is not to be mistaken with the average density of mobile dislocations used in the Orowan's equation (ρ) (see Hirth and Lothe, 1982, Zoller et al., 2021). The later would be the sum of the GND and the statistically stored dislocations (SSD) which includes loops, dipoles, or multipoles, if they are mobile and not locked into the crystal (e.g., by impurities). As the SSD are producing a null Burgers vector and do not modify the curvature of the crystallographic lattice, they cannot be identified with the method used here, while they can be identified and quantified by transmission electron microscopy. Therefore, GND is, by definition, an imperfect proxy for total mobile (free) dislocations (cf. Orowan's equation) producing plastic deformation by dislocation glide. GND can only represent a fraction of the elastic energy still stored in the crystal lattice after sample quench. In this study as in others (e.g., Cordier et al., 2014, Wallis et al., 2016; Hansen et al., 2021), we will hypothesize a proportionality relationship between GND density and the total (average) mobile dislocations density accommodating the strain. While GND and SSD are unambiguously related (Mughrabi, 2001), recent study in work-hardened two-phase metals (ferrite/bainite) showed that their relationship is very complex and a function of pre-existent microstructures and increasing strain (e.g., Wang et al., 2022).

155 Here, the Nye's tensor (in μm^{-1}) is calculated and represents the density of Burgers vectors per unit surface. First the Nye's tensor is calculated in the map coordinate system as follows,

$$\alpha_{ij} = b_i t_j \tag{1}$$

with b the Burgers vector surface density and t the unit line direction of the corresponding dislocation (screw dislocation when colinear, edge dislocation when orthogonal to each other). This matrix is then rotated to be placed in the

160 crystal frame α_{ij}^c denoted by a superscript ‘c’. For simple cubic structure such as metals, having a unique b yields a simple relation as in metal sciences, but which remain a mere convention. The density is expressed as

$$\rho_\alpha = \frac{1}{b} \|\alpha_{ij}\| \quad (2)$$

and with the norm of GND density defines as

$$\|\alpha_{ij}\| = \sqrt{\alpha_{ij} \cdot \alpha_{ij}} \quad (3)$$

165 The Nye’s tensor is obtained in μm^{-1} and ρ_α converted in m^{-2} (Table S1) by dividing them by the magnitude of the burgers vector b (which is different for each slip system in olivine, e.g., if $b = 4.764 \text{ \AA}$ for [100] dislocation, then $1 \mu\text{m}^{-1}$ corresponds to $2.1 \times 10^{15} \text{ m}^{-2}$). Here, we chose not to follow this mere convention, and to divide the density by the EBSD map step size (*step*) to yield a proper dislocation length per volume unit, which are reported in Table 2 (also given in Table S1).

$$\rho_\alpha^c = \sum_{i,j} \frac{|\alpha_{ij}^c|}{step} \quad (4)$$

170 We recall that only five Nye’s components out of nine can be calculated from the two-dimensional EBSD map ($\alpha_{12}, \alpha_{13}, \alpha_{21}, \alpha_{23}$, and α_{33}), the other four are non-determined components ($\alpha_{11}, \alpha_{22}, \alpha_{31}$, and α_{32}) of unknown value and here a value equal to 0 is taken for each of them for the calculation in the crystallographic framework. Subsequently, nine components in the crystallographic framework (α_{ij}^c) can be calculated following

$$\alpha_{ij}^c = P^T \alpha_{ij} P \quad (5)$$

175 Where P is the rotation matrix and P^T is the transpose of the rotation matrix. Note that the nine resulting components have the same level of uncertainty.

2.2.3 Disclination detection, densities and display

We recall in Figure 1 how disclination densities are calculated from the elastic rotation field ω_e along (and not across) a grain boundary. In this example, there are two crystals with orientations given by Euler angles of $(0^\circ, 0^\circ, 0^\circ)$ and $(45^\circ, 0^\circ, 0^\circ)$ and a subgrain (in turquoise blue in fig. 1 into Grain 1a) is inserted into the top grain with a tilt disorientation of 3° around the axis e_3 (corresponding to Euler angles $(3^\circ; 0, 0)$). The K_{31}^e component of the curvature tensor (i.e., curvature field K_{ij}^e) is derived by one-sided differentiation of the corresponding component of the elastic rotation vector ω_3^e (i.e., the elastic rotation field), which is illustrated in Fig. 1b, while the curvature field K_{32}^e is then derived by the forward differentiation of ω_3^e as well. Finally, the density of wedge disclinations θ_{33} is derived from the forward differentiation of the curvature fields K_{31}^e and K_{32}^e (Fressengeas and Beausir, 2018). The resulting pair of positive (color-coded red) and negative (color-coded blue) wedge disclinations thus forms a dipole, which terminates at the sub-grain boundary reaching the grain boundary and therefore bridges the discontinuity of 3° in elastic rotation along this interface. To avoid potential artifacts created at grain boundary steps (e.g., pixelization) and the inherent calculation of the rotation gradients variation on a stepped boundary, disclinations

185

are calculated only for portion of straight horizontal or straight vertical grain boundaries (e.g., Fressengeas and Beausir, 190 2018).

An application of this calculation is shown in Figure 2 for the small section of the starting material EBSD map (sample CMT16-7), where disorientation gradient pixel per pixel can be seen along olivine grain boundaries. As this scale of investigation is impractical to compare large EBSD maps, smoothing is applied to ease display and to reach a certain visual comfort (i.e., compatible with publication format). Smoothing too much strongly affects the displayed width of disclinations 195 monopoles and dipoles as shown by Figure 2b-e, till the point where it gives the false impression that the disclination is ‘cross-cutting’ the grain boundary. Nonetheless, only non-smoothed data are used for the density calculations (Fig. 2a). A smoothing factor of 2 was found appropriate to yield the best display of the EBSD maps investigated here.

While the chosen smoothing treatment does not impact disclination densities, the chosen range of disorientation e.g., 0 - 1°, 0 - 5°, or 0 - 10° does impact the output disclination densities. Indeed, as expected a larger disorientation range (0- 200 10°) yields higher disclination densities than a restrain range (e.g. 0-5°) as it acts as a cut-off. Furthermore, a fine range of disorientation (0 - 1°) is a necessity to visualize disclinations along sub-grain boundaries, and large range of disorientation (0-25°) only highlights major disclinations at triple junctions (major subgrain boundaries). The effect of disorientation range for disclination identification (and thus quantification) is illustrated by Figure 3 on a relatively large olivine grain (6-8 μm), with cross-cutting subgrain boundaries in the selected area of starting material (CMT16-7, left edge of the original map). A 205 range of 0 – 10° of disorientation is found appropriate for our samples to best identify the disclination population along the grain boundaries. This choice is also consistent with the 10° used to define grain boundaries.

Once disclinations are detected, the densities can be calculated, but from a two-dimensional map, only θ_{13} , θ_{23} and θ_{33} can be obtained. Nevertheless, we emphasis that to date ATEX is the only software able to provide such quantification. The average disclination density is noted ρ_θ and correspond to the entrywise norm of the respective matrix. As mentioned above, 210 the maps are only two-dimensional, thus we stress that the entrywise norm is only a partial representation of the ‘true’ disclination density (three non-null components out of nine components), not rotated in the crystal framework. Nevertheless, the entrywise norms obtained in the sample framework or crystallographic framework yield identical values. As the crystallographic control on Frank’s vector (ω) and its magnitude are still unknown for olivine, in the simplified system considered here, we take,

$$215 \quad \theta_{ij} = e_{jkl} \kappa_{il,k}^e \quad (6)$$

$$\rho_\theta = \sqrt{(\theta_{13}^2 + \theta_{23}^2 + \theta_{33}^2)} \quad (7)$$

We recommend to adjust the scale individually (user-defined mode) for each map first, before choosing a common user-defined scale. Sample area with very low disclination densities blend in with the colored background. Adjustment and trade-offs are a necessity to best visualize the treated maps. For our set of maps, the best set up is a range of disorientation 0- 220 10° (as defined for grain boundary) and a user-defined scale of -0.5 to +0.5 rad.μm⁻² for disclination norms. As for the

smoothing factor, the choice of auto-scale or user-defined scale (linear or log) does not affect the calculated GND or disclination densities, only the display is affected.

For EBSD maps which were acquired at step sizes $< 0.1 \mu\text{m}$ (Table 2), ρ_{α}^c and ρ_{θ} were calculated for the original step size. Furthermore, the same maps were sampled again and only every second pixel was kept for analysis to reach $0.1 \mu\text{m}$ of step size and to permit accurate comparison with the other EBSD maps. Furthermore, the map sample CMT16-13_SII was sampled again for a step size of $0.2 \mu\text{m}$ to further assess the importance of step size on both ρ_{α}^c and ρ_{θ} quantification. At last, ATEX can generate statistics of GND and DCL (1) per pixel and (2) per grain (one point per grain: oppg). Resulting densities for a given map are not identical. The average oppg density per map based on average density per grain can be calculated, but we also provide the median per map. Comparison between average and median densities show that average density per map overestimate densities compare to median densities (see Table 2).

2.2.4 Numerical estimation of internal elastic energy induced by GND and disclination densities

To further probe the relative roles of dislocations and disclinations in the accommodation of plastic deformation, we will use the GND and disclination densities, as measured by EBSD, as inputs in two-dimensional Field Dislocation and Disclination Mechanics (FDDM) simulations previously developed by Fressengeas et al (2011). The field equations (incompatibility equations, balance of stress equation) are numerically solved with Fast Fourier Transform (FFT) based spectral solvers, and methodological details can be found in previous studies (Berbenni et al, 2014; Djaka et al, 2017; Berbenni and Taupin, 2018). In the simulations presented later, the FFT grid size is the same as the EBSD map step size. For a given region of interest selected on a EBSD map, inputs in the simulations will be the orientation of each grain (Euler angles) and the GND and disclination densities. Elastic coefficients in the olivine crystal frame (*Pbnm*) are $C_{1111}=320.2$ GPa, $C_{2222}=195.9$ GPa, $C_{3333}=233.8$ GPa, $C_{2323}=63.5$ GPa, $C_{1313}=76.9$ GPa, $C_{1212}=78.1$ GPa, $C_{1122}=67.9$ GPa, $C_{1133}=70.5$ GPa and $C_{2233}=78.5$ GPa (as in Cordier et al, 2014). For a selected EBSD map, four different simulations will be run, namely (i) a simulation with no defect, but with applied axial loading (like the experimental one) to see the effect of crystalline elastic anisotropy on the distribution of energy, (ii) a simulation with only GND densities and no loading, (iii) a simulation with only disclination densities and no loading, and (iv) a simulation with both GND and disclination densities and no loading. In the simulations with no loading, all stress components are imposed to be null macroscopically (only one component is assigned to a very small value to ensure convergence of the spectral algorithm). Periodic boundary conditions are present in all directions due to the use of Fourier transforms. As such, care is to be taken in the analysis of the simulated mechanical fields distribution, one should rather consider fields in the center of the simulation domains and not those near the map boundaries. Nevertheless, the predicted mechanical fields allow here to investigate qualitatively the concurrent role of GND and disclination densities in accommodating plastic deformation of olivine. From initial dislocation/disclination inputs, the FDDM simulations will give here as outputs the elastic strains and rotations, the internal stresses (Cauchy stress tensor), the elastic curvatures and the local elastic energy density in the microstructure modeled. Note that FDDM can further be used to

255 simulate the transport of defect densities during plastic straining. In this preliminary FDDM analysis, we will compare the distributions of the internal elastic energy for the four cases mentioned above, to evidence the interplay between disclinations and dislocations.

3 Results

3.1 Microstructures

260 We compile below the statistical results from the new EBSD investigation; it is a complement from previous studies (Demouchy et al., 2012; Thieme et al., 2018), not a duplicate. Forward scattered electron images representative of the starting material (CMT16-7), samples from uniaxial compression at 1000 °C (CMT17-2), from uniaxial compression at 1200 °C (CMT16-9) and from torsion experiment at 1200 °C (PI0546) are presented in Figure 4. All samples are composed of olivine at 99.8 %, enstatite and Cr-spinel only represent < 0.2 % in the studied area. Grains are sub-equant; the average
265 olivine grain size is homogeneous trough the data set and range from 1.3 to 2.7 μm . The mean aspect ratio is 1.4–1.5 and maximum aspect ratios are up to ~ 3.0 . Grain boundaries are curved and/or serrated and only a hint for grain boundary migration is observed (i.e. grain growth at the expense of the most highly misoriented neighboring grains), which is also observed in the starting material (CMT16-7, Fig. 4a). Few grains show residual internal micro-cracks oriented at 60 ° to each other, that are also present in the starting material and which are attributed to thermal cracking during rapid quench. Indeed,
270 there is no significant displacement or sliding along these cracks. A low fraction of porosity (2-5 %) is apparent in Figure 4, which is mostly inherited from the notorious imperfect hot-pressing at 300 MPa even for very fine grain size of olivine (e.g., Beeman and Kohlstedt, 1993; Zimmerman and Kohlstedt, 2004; Demouchy et al., 2014; Hansen et al., 2012; Warren and Hirth, 2006). The initial low porosity is also overestimated because of grains plucking during the polishing stages.

275 The conditions of the deformation experiments and mechanical results are recalled in Table 1, while the new acquisition indexation rate, step size, number of identified grains, average grain size, ρ_{α}^c and ρ_{θ} for each of the 19 EBSD maps are given in Table 2. The indexation rates for our EBSD maps are at least 90.9 % and up to 97.9%.

3.2 GND and disclinations identification and their densities

280 An example of GND identification and distribution in the crystallographic frame is provided in Figure 5 for sample PI0456- XIV (full map displayed). Dislocation types in the crystallographic framework (α_{ij}^c) and corresponding olivine slip systems ([uvw](hkl)) are both indicated in the figure. The correspondence is recalled in Table 3, but only for the main slip systems in olivine (see further details in Mussi et al., 2014). GND distribution is heterogeneous and as expected, the highest densities are observed along well-developed sub-grain boundaries, but with a mixed character, made of both [100] and [001]
285 dislocations. From the full data set, the average oppg GND density ranges between $2.25 \times 10^{11} \text{ m}^{-2}$ and $5.28 \times 10^{11} \text{ m}^{-2}$ (Table 2 for 0.1 μm step size). One of the minimal dislocation densities is found for the starting material which is $2.6 \times 10^{11} \text{ m}^{-2}$. The

same distribution is found when comparing median values (Table 2). The highest density is observed in a sample deformed at low temperature and high stress (1000 °C, sample CMT17-2). Note that the minimum dislocation density from all maps (0.1 μm step size) is $2.0 \times 10^{10} \text{ m}^{-2}$ in average. Furthermore, average α_{1j}^c densities are rather similar to α_{3j}^c (Table S1). The
290 GND densities do not clearly vary between samples deformed in uniaxial compression or in torsion with comparable stresses, finite strains and number of grains (Table 2). The most deformed sample at 1000 °C (CMT17-2) has a higher GND density than the most deformed sample at 1200 °C (CMT16-9) for similar strain rate ($\sim 1 \times 10^{-5} \text{ s}^{-1}$), and both have higher GND densities than the starting material (Table 2).

From the same sample (PI0456-XIV), typical disclination type and spatial distribution are shown in Figure 6.
295 Disclination monopoles and dipoles are located along grain boundaries, and with a distinctive occurrence at junction between a sub-grain boundary and a grain boundary (black arrows in Figures 3 and 6). Furthermore, disclinations are also found at the intracrystalline tip of subgrain boundaries (pink arrows) as shown in both the starting material (Fig. 3) and in experimentally deformed samples. We show another example in Figure 7, but for a larger range of disorientation for disclinations detection. For a distinctive range of disorientation (e.g., 0.1° or $0-5^\circ$), disclinations can occur as strings of
300 monopoles along subgrain boundaries (Fig. 3b). Overall, through the data set, the oppg disclination density ranges from 7.3×10^{-3} to 6.5×10^{-2} to $\text{rad } \mu\text{m}^{-2}$ (Table 2). As for GNDs, there is no clear variation (increase or decrease) between samples deformed in uniaxial compression or in torsion with comparable stresses. However, the most deformed sample at 1000 °C (CMT17-2) has a higher disclination density than the most deformed sample at 1200 °C (CMT16-9) for similar strain rate ($\sim 1 \times 10^{-5} \text{ s}^{-1}$), but only by a factor of 1.4.

305

3.3 Impact of step size

For both GNDs and disclinations, a special attention was given to the impact of step size for accurate comparison while keeping step size small enough ($\leq 0.1 \mu\text{m}$) for accurate detection of variation of the disorientation gradient along grain boundaries. The effect of the step size on the resulting GND and disclination densities is shown in Figure 8. As expected,
310 both GND and disclination densities are strongly dependent on the spatial resolution of the EBSD map. Here GND and disclination distributions are shown for sampling at a larger step size of 0.1 and 0.2 μm . The maps are displayed here with a fixed user-defined scale (i.e., -0.5 to $+0.5 \mu\text{m}^{-1}$ for GND and -0.5 to $+0.5 \text{ rad} \cdot \mu\text{m}^{-2}$ for disclination). We selected to show α_{31}^c corresponding to edge $[001](100)$ dislocations as an example here, but similar decrease in dislocation density is observed for α_{1j}^c (cf. Table S1). Disclination θ_{33} is chosen again for the illustration of the acquisition step size impact. Doubling the step
315 size twice (from 0.05 to 0.2 μm) results in a decrease by a factor 4 for ρ_α^c and a drastic decrease by a factor 16 for ρ_θ as reported in Table 2 and displayed in Figure 9. The decrease is not linear, clearly showing the necessity of very fine step size ($\leq 0.1 \mu\text{m}$) compared to the commonly used 0.25-1.0 μm step size (even with high angular resolution EBSD e.g., Wallis et al., 2016; 2017). This result also illustrates the difficult trade-off between spatial resolution ($\leq 0.1 \mu\text{m}$) and the final size of the EBSD map to properly characterize a sample with a sound statistical meaning.

3.4 GND distribution and grain size

While the average grain size is small (2 μm) and relatively homogeneous across the data set, we tentatively explore the relationship between the GND population and the grain size for this limited grain size range (0.2-20 μm). The oppg GND densities in olivine as a function of grain size is displayed in Figure 10a for four maps (all for a step size of 0.1 μm) from the starting material (CTM16-7), the sample deformed in axial compression at low temperature (1000 $^{\circ}\text{C}$) and highest stress (CMT17-2), the sample deformed in axial compression at high temperature (1200 $^{\circ}\text{C}$) and highest strain (CMT16-9) and for one sample deformed in torsion for the largest maps (PI0546-III, over 770 grains). The corresponding data set is given in Tables S1. The data are scattered and do not show a distinct correlation between oppg GND densities and grain size. However, the average oppg GND density in the starting material is lower ($2.6 \times 10^{11} \text{ m}^{-2}$) than in the deformed sample in compression (CMT17-2 SII-sample, $5.3 \times 10^{11} \text{ m}^{-2}$ and CMT16-9 SII-sample, $3.6 \times 10^{11} \text{ m}^{-2}$) or in the deformed sample in torsion (PI0546-III sample, $3.9 \times 10^{11} \text{ m}^{-2}$). The difference in oppg GND density is less than one order of magnitude, though it approaches a substantial factor 2. Furthermore, if GND densities are normalized to the grain size, a negative correlation is found, as shown in Figure 10b (following $y=x^{-1}$), it is not suggesting that GND are mostly present in small grains but reflect heterogeneity in the GND distribution, especially in the large grain and thus a dilution effect. For the four samples considered in Figure 10a,b, we further show the distributions of the average GND density per grain in Figure 10c (for a fixed number of bins of 50, whatever the number of grains), which demonstrates a distribution close to a log normal one, and which indicates that the use of a median value instead of a crude average from average per grain would be preferable (see Table 2 and Table S1 for numerical values comparison).

While the extracted densities permit to explore limited statistical parameters, one of the complementary approaches is also to compare dislocation distributions in maps visually. Does one can see in the maps the dislocation density difference observed in average and median densities between the low and high temperature deformation in axial compression? We illustrate the answer with in Figure 11, which shows two ways to display the GND norm. Fig. 11a and b are identical and Figures 11c and 11d are also identical. Only the color scale is different; in blue, we used the classic color scale ‘Jet’ of Matlab (rainbow, starting with blue, with a smoothing factor of 2), also used for typically for KAM maps and in green a log scale (linear green in ATEX, with a smoothing factor of 1). A higher density in GND and more grains with numerous GNDs for the sample deformed at lower temperature are visible in Figure 11, confirming the veracity of value extracted from the map (Table 2). Furthermore, one can easily differentiate two populations of GND with the green color scale while they remain very subtle using the classic blue color scale. A major one (white arrows), defining, as expected, the well-defined subgrain boundaries, but also a second population, widespread (e.g., dashed black circle), not homogeneous but practically ubiquitous, defining an almost polygonal structure similar to the one observed during dynamic recrystallization (Fig. 11). High temperature sample still displays GND-poor small grains while in the sample deformed at low temperature, even small grains have high GND densities. Even if GND are a mere proxy for average mobile dislocation, in this specific case and

qualitatively, the method remains discriminant and in agreement with Orowan's law. Although, the reliability of the numerical densities remains to be examined.

355

3.5 Disclination distribution and grain size

Since disclinations are distributed along grain boundaries or at subgrains, correlations between the oppg disclination densities and grain size is expected. To further assess the role of grain boundary network (or grain size) in disclination abundance, oppg disclination density is shown as a function of grain size or grain perimeter in Figure 12a, and demonstrates a negative correlation (following $y=x^{-1}+b$). Furthermore, disclination densities are normalized to the perimeter (for a hypothetical spherical grain of diameter D with equal area than the given grain) of each grain (thus in μm^{-3}) as a function of the grain perimeter. The results is provided in Figure 12b to compare small and large grains. The oppg disclination densities is again inversely correlated to grain perimeter for the four samples already selected for Figure 10. A linear least square fit through the log-log data for each sample yields a relationship with the starting material. The latter displays an oppg normalized disclination density $f(x) = x^{-1.8} \times 10^{-1.63}$, slightly lower than for the three deformed sample for similar perimeters range. Moreover, the global fit through the three oppg deformed sample sets, yields a distribution following $f(x) = x^{-2} \times 10^{-1.3}$. This first approximation emphasizes the predominant occurrence of disclinations along boundaries in the smallest grains, even in the absence of noticeable dynamic recrystallization in this very fine-grained olivine aggregates (cf., Thieme, et al., 2018). This result also shows a noticeable difference between the oppg disclination density of starting material (in CMT16-7, median value, $\rho_\theta = 4.08 \times 10^{-3} \text{ rad} \cdot \mu\text{m}^{-2}$) and of the deformed polycrystalline olivine (in PI0548, $\rho_\theta = 7.12 \times 10^{-3} \text{ rad} \cdot \mu\text{m}^{-2}$). However, there is a negligible difference between the results from low and high temperature experiments in compression or torsion (median values for CMT17-2, $\rho_\theta = 1.11 \times 10^{-2} \text{ rad} \cdot \mu\text{m}^{-2}$; CMT16-9 $\rho_\theta = 7.54 \times 10^{-3} \text{ rad} \cdot \mu\text{m}^{-2}$; PI0548, $\rho_\theta = 7.12 \text{ rad} \cdot \mu\text{m}^{-2}$). The inverse correlation thus suggests that small grains would bare more disclination than relatively large grains in these fined-grain olivine samples, deformed or not deformed.

375

3.6 GND and Disclination correlation

GND are usually seen as an indicator of the ductile deformation experienced by a polycrystalline material assuming that dislocation motion is the dominating parameter controlling creep and that a proportionality between GND and SSD is established (cf. Orowan's law, Hirth and Lothe, 1982; Wang et al., 2022). Since disclinations are also 1-dimentional defects accommodating strain, and that we are now able to detect and quantify them, it is legitimate to question the respective role of these two types of defects (dislocations and disclinations) in the production of the strain and crystalline misorientation. Thus, we compare the GND and disclination densities both normalized to grain size for sample PI-0546, in Figure 13. Since in these deformation experiments, GND densities are not strongly dependent on grain size (Figure 10a, b), the resulting positive correlation is mostly driven by the grain size dependence of disclination densities (Fig. 12). We remind that the average

385 grain size in our samples is rather small (2-3 μm), thus such correlation would need to be confirmed by studying a wider
range of range sizes and if possible, up to geological relevant olivine grain size (2-10 mm).

4 Discussion

4.1 Occurrence of GNDs, comparison with previous studies

390 The calculation of the Nye's tensor, followed by the rotation in the crystallographic frame of each grain permits to identify
the type of dislocations composing subgrain boundaries and the results show that, as expected, subgrain boundaries are
mostly built with dislocations of both [100] and [001] Burgers vectors, resulting in a boundary with a mixed character,
(neither perfect twist or tilt) as reported previously (e.g., Cordier et al., 2014; Wallis et al., 2017; Lopez-Sanchez et al.,
2021). Despite the extremely rare to non-presence of [010] dislocation in olivine, here dislocations of the type $\rho\alpha^c_{2j}$ are
present in the output results, with often a factor 2 of difference as compared to $\rho\alpha^c_{1j}$ or $\rho\alpha^c_{3j}$ (Table S1). This result is at odds
395 with decades of TEM investigations, but agrees with other EBSD studies mapping the Nye's tensor (e.g., dislocations ' α_{2j} ' in
Fig. 2c in Cordier et al., 2014 ; dislocations ' α_{23} ' in Fig. 1 in Wallis et al., 2016). Here, we suggest that the occurrence of α^c_{2j}
dislocations is interpreted as mere contributions from α^c_{11} and α^c_{33} screw dislocations components and not as a proof of the
existence of dislocations with such a long Burgers vector (cf. $|\vec{b}_i| = 10.22 \text{ \AA}$).

400 Furthermore, the distribution of the entrywise norm, (Figure 11, see also Figure S1) still permits to infer the
presence of additional GND in-between the array of major GND (cf. subgrain boundaries), but these GND have different
spatial distribution than the well-oriented subgrain boundaries within a given grain. A straightforward comparison of minor
GNDs distribution between the polycrystalline sample deformed at 1000 $^\circ\text{C}$ and high stress (1073 MPa, CMT17-2) and the
polycrystalline sample deformed at high temperature and lower stress (322 MPa, sample CMT16-9) for at similar strain rate
($\sim 1 \cdot 10^{-5} \text{ s}^{-1}$) and level of strain (7.3-8.6 %) agrees with what is known from the hardening phenomenon during creep
405 mechanism at low temperature in olivine (800-1050 $^\circ\text{C}$). At these temperatures, recovery mechanisms (e.g., ionic self-
diffusion, climb) are not efficient enough when compared to high temperature creep (e.g., Raleigh, 1968; Demouchy et al.,
2013, 2014; Mussi et al., 2015; Gouriet et al., 2019). While minor GND populations are now visible, the level of details
provided by high angular EBSD is of course not achieved here (Wallis, et al., 2016, 2017, 2022), in particular the clear
doubling aspect of parallel GND bands having positive and negative signs (e.g., Figure 6 in Wallis et al., 2017; or Figure 5a
410 in Wallis et al., 2022). Nevertheless, our results still permit to obtain a better resolution and an enriched information when
compared to the classic decoration technique (Kohlstedt, 1976) at a scale larger than conventional TEM investigations. The
spatial resolution permit here to appreciate finer details in GND distribution, but we obtain similar information than from
recent studies from olivine single crystals (e.g., Faul, 2021) deformed at higher temperature (1600 $^\circ\text{C}$). Moreover, the
method reported here (treatment and display set up) represent an improvement when compared to conventional EBSD
415 mapping and post-data treatment and display (e.g., Demouchy et al., 2014; Thieme et al., 2018, Gasc, et al., 2019).

4.2 Relationship between disclinations and grain size

We have shown that disclinations are found ubiquitously in each EBSD map, regardless of the finite strain or stress (Table 2) and, as expected, the calculated disclination densities strongly depends on the EBSD acquisition step size (Fig. 9).
420 Furthermore, we recommend to always give the step size when disclinations or GND densities quantification are the main aim. For identification, a step size of 0.1 μm or even less is considered here as a good compromise (map size, spatial resolution) for detailed maps at the grain scale (10-100 grains). Moreover, for the same step size (0.1 μm), we did not find that the mechanical strength of olivine is positively correlated to a drastic variation (increase or decrease) of the average oppg disclination density (Fig. 13). Disclinations and dislocations are correlated (Fig. 13) as they are both the expression of
425 misorientation that allows to accommodate elastic strain, but this result does not explicitly give the efficiency of disclinations as a companion accommodation mechanism of the ductile deformation. The most striking feature is the inverse correlation between the disclination density and the grain size or perimeter (a proxy representing the grain boundary network) as shown in Fig. 12a which yields a simplified relationship to the grain size as follow,

$$\rho_{\theta} \approx \pi d^{-1} \times 10^{-1} \quad (8)$$

430 where d is the grain size (μm). Such inverse correlation is common for deformation mechanisms strongly function of the grain size (grain boundary sliding, diffusion creep), and also found in paleopiezometers (e.g., Gueguen and Darot, 1980). For example, we recall the relationship reported by Gueguen and Darot (1980) between the dislocation density obtained by decoration (GND + SSD) and the dislocation walls spacing: $\rho_{\alpha}^{deco} \approx S^{-0.7} \times 10^{0.163}$ (their figure 6), which thus shows a similar dependence between 1-dimensional defect density and a proxy of grain size, but for natural olivine and thus with
435 larger grain size. Here, unfortunately, we do not have a range of data large enough to investigate the strain rate- or stress-dependence, but it is still an indication that disclination development is more prominent in very small grains than in larger grains, where dislocation development would be less favorable (e.g., Miyazaki et al., 2013).

To decipher the potential interaction or relationship between GND and disclination, we surimpose a misorientation map with disclination density θ_{33} in Figure 14. Three types of disclination contexts (dipole or monopoles) can be identified.
440 First (yellow arrow), important disclinations at the junction of subgrain boundaries (plotted in pink here for clarity) and grain boundaries (in dark green). Second (orange arrow), disclinations located along grain boundary in the zone of important misorientation, in the prolongation of a subgrain boundary in construction, but with a misorientation lower than the 10° defining subgrain boundaries. Third (red arrow), a type of disclination population, more pervasive located in large grains with high misorientation but also in small grains (homogeneous pale blue) apparently not associated with significant
445 variations in the misorientation. This latter observation suggests a precursor role of disclination compared to GND, which will need to be confirmed by dedicated deformation experiments and high angular EBSD mapping. Nonetheless, these observations further confirm that disclinations are companion of dislocations in plastically deformed olivine and can allow rotation of very small crystal volumes in very small olivine grains when dislocation could not be formed yet easily.

450 4.3 Elastic energy distribution: GND and disclination interactions

To clarify the potential interactions between GND and disclinations, we now present the FDDM simulation predictions using the GND and disclination densities obtained from EBSD maps as inputs. The elastic energy distribution in the aggregate deformed axially (with 1000 MPa of applied macroscopic compressive stress, as for low temperature experiments Thieme et al., 2018, Gasc et al., 2019), is shown in Figure 15a. The resulting map shows the mechanical incompatibilities coming from elastic anisotropy and different olivine crystallographic orientations in grains for a section of CMT16_9 (same as in Fig. 14). The stored energy distribution from GND only is shown in Figure 15b, and from disclinations only in Figure 15c. The energy obtained with both types of defects is finally shown in Figure 15d. GND and disclinations do not yield the same energy distributions and they also highlight different areas of the sample aggregate. The GND energy majorly appears concentrated in a few grains around a larger grain size, with a maximum of 400 J/m^3 , while the disclination energy is generally more diffuse in the aggregate, with a few “hotspots” with a maximum around 800 J/m^3 . Moreover, when both defects are simultaneously considered, the energy level and then the distribution is logically controlled by disclinations (Fig. 15d), but several areas display a reduced total energy is reduced (blue arrows in Figure 15d), while in other areas, the energy builds up (pink arrows in Figure 15d). These maps thus permit to infer rather complex interactions between GND and disclinations and motivates future analysis.

465

4.4 Methodological limitations and potential application to natural peridotite specimens

Despite using conventional EBSD and not high-angular resolution EBSD, the treated EBSD maps presented in this study permit to identify and quantify new populations of defects in olivine (minor GND and disclinations). A logical improvement would be the combination with high-angular resolution EBSD, based on the transmission Kikuchi diffraction and simulated electron backscatter pattern combined with digital image correlation (e.g., Britton and Wilkinson, 2011 ; Wallis et al., 2016). However, for neither of these three techniques, the size of EBSD maps (e.g., $500 \times 500 \mu\text{m}$) which can be acquired and treated is far smaller than the size of a regular petrological section (e.g., $45 \times 30 \text{ mm}$). It also requires significant acquisition time (often $>10 \text{ h}$) and generates a large octet size ($\gg 20 \text{ Mo}$). Therefore, the methodology reported in this study must be seen as a complementary technique to locally decipher mechanisms of deformation since it is not statistically as powerful as than conventional EBSD maps on regular rock section (> 500 grains of mm size). However, this technical limitation is nevertheless going to be improved with increasing calculation capacity and decreasing data acquisition time. Another limitation is the exactness of the output values. Since we have only 5 components out of 9 in the Nye’s tensor only, thus the GND, and the disclination densities (3 components) are only a partial (*a minima*) density and will never be absolute values. Thus, potential strain evaluation or stress (after application of Hooke’s law) extracted from such data are only partial values related to the local elastic energy which are poorly related to what is happening at macroscale (e.g., stress-strain curve of deformed centimetric sample). Each treated EBSD map must then be interpreted with care when compared to each other or regarding its mechanical data.

480

5 Conclusions

485

In this paper we report GND and disclination densities in deformed polycrystalline olivine from a broad range of experimental conditions. Based on the new dataset, we find that (1) GND form subgrain boundaries of mixed character, but also a secondary pervasive network, (2) the disclination monopoles and dipoles are observed along grain boundaries in non-deformed and deformed samples, and (3) disclination densities appear independent of bulk stress, or strain, or even
490 temperature of deformation. Nevertheless, (4) the disclination density is inversely correlated to grains size, suggesting that the action of disclinations compensate the lack of dislocation motions in the smallest grains; (5) detailed observation of selected areas of EBSD maps suggest that disclinations could act as precursor of GND during the formation of misorientations and (6) could also interact with GND. At last, our results support that disclinations act as a plastic deformation mechanism, by allowing rotation of a very small crystal volume.

495

Author contribution: SD designed the project and the deformation experiments and MT carried them out. EBSD analyses were performed by MT under the supervision of FB and SD. Data treatment were performed by MT and SD, BB developed the ATEX code and BB and VT performed the elastic energy simulations. SD prepared the manuscript with contributions from all co-authors.

500

Competing interests : The authors declare that they have no conflict of interest.

Acknowledgements

We acknowledge funding from the European Union's Horizon 2020 research and innovation program under the Marie Skłodowska-Curie Grant agreement No. 642029 (ITN CREEP); as well as CNRS-INSU through their program TELLUS-Syster (project DOMINO 2021-2022) and the European Research Council (ERC) under the European Union's Horizon 2020 research and innovation program under grant agreement No 787198 – TimeMan. SD thank C. Nevado and D. Delmas for providing high-quality thin sections for EBSD and C. Thoraval, T. Menand for constructive inputs. SD deeply thank C. Fressengeas for crucial meeting at Metz Plasticité conference in 2012. The SEM-EBSD facility at Montpellier University is
510 supported by the Institut National de Sciences de l'Univers (INSU) from Centre National de la Recherche Scientifique (CNRS, France) and the Conseil Régional d'Occitanie (France). ATEX is available at <http://atex-software.eu>. EBSD data (.ctf) used to generate the ATEX maps presented in supplementary material S1 are available at the Zenodo Open Aire repository under the doi:(*to be added after the first round of review*).

References

- 515 Bachmann, F., Hielscher, R. and Schaeben, H.: Texture Analysis with MTEX - Free and Open Source Software Toolbox, in: Klein, H., Schwarzer, R.A. (Eds.). Presented at the Texture and Anisotropy of Polycrystals III, Trans. Tech. Pub. Ltd. Durnten-Zurich Swizerland, p. 63. doi:10.4028/www.scientific.net/SSP.160.63, 2010.
- Bernard, R.E., Behr, W.M., Becker, T.W. and Young, D.J.: Relationships Between Olivine CPO and Deformation Parameters in Naturally Deformed Rocks and Implications for Mantle Seismic Anisotropy. *Geochem. Geophys. Geosys.* 20, 3469–3494. doi:10.1029/2019GC008289, 2019.
- 520 Beusir, B. and Fressengeas, C.: Disclination densities from EBSD orientation mapping. *Int. J. Solids Struct.* 50, 137–146. doi: [10.1016/j.ijsolstr.2012.09.016](https://doi.org/10.1016/j.ijsolstr.2012.09.016), 2013.
- Beusir B. and J.-J. Fundenberger, Analysis Tools For Electron And X-ray diffraction, ATEX - software, www.atex-software.eu, Université de Lorraine - Metz, 2017
- 525 Beeman, M.L. and Kohlstedt, D.L.: Deformation of fine-grained aggregates of olivine plus melt at high temperatures and pressures. *J. Geophys. Res.* 98, 6443–6452. doi: [10.1029/92JB02697](https://doi.org/10.1029/92JB02697), 1993.
- Berbenni, S., Taupin, V., Djaka, K.S. and Fressengeas, C.: A numerical spectral approach for solving elasto-static dislocation and g-disclination mechanics, *Int. J. Solids Structures* 51, 4157-4175, doi: [10.1016/j.ijsolstr.2014.08/009](https://doi.org/10.1016/j.ijsolstr.2014.08/009), 2014.
- 530 Berbenni, S., and Taupin, V.: Fast Fourier transform-based micromechanics of interfacial line defects in crystalline materials, *J. Micromechanics Molecular Physics* 3, doi:10.1142/S2424913018400076, 2018.
- Britton, T.B. and Wilkinson, A.J.: Measurement of residual elastic strain and lattice rotations with high resolution electron backscatter diffraction. *Ultramicroscopy* 111, 1395–1404. doi:10.1016/j.ultramic.2011.05.007, 2011.
- Buening, D.K. and Buseck, P.R.: Fe-Mg lattice diffusion in olivine. *J. Geophys. Res.* 78, 6852–6862. doi: <http://dx.doi.org/10.1029/JB078i029p06852>, 1973.
- 535 Cordier, P., Demouchy, S., Beusir, B., Taupin, V., Barou, F. and Fressengeas, C.: Disclinations provide the missing mechanism for deforming olivine-rich rocks in the mantle. *Nature* 507, 51–56. doi: [10.1038/nature13043](https://doi.org/10.1038/nature13043), 2014
- Demouchy, S.: 2010. Diffusion of hydrogen in olivine grain boundaries and implications for the survival of water-rich zones in the Earth's mantle. *Earth Planet. Sci. Lett.* 295, 305–313. doi: [10.1016/j.epsl.2010.04.019](https://doi.org/10.1016/j.epsl.2010.04.019), 2010.
- 540 Demouchy, S.: Defects in Olivine. Invited review article. *Eur. J. Mineral.* 33, 249-282, doi: [10.5194/ejm-33-249-2021](https://doi.org/10.5194/ejm-33-249-2021), 2021.
- Demouchy, S., Mussi, A., Barou, F., Tommasi, A. and Cordier, P.: Viscoplasticity of polycrystalline olivine experimentally deformed at high pressure and 900°C. *Tectonophysics* 623, 123–135. doi:10.1016/j.tecto.2014.03.022, 2014.
- Demouchy, S., Tommasi, A., Ballaran, T.B. and Cordier, P.: Low strength of Earth's uppermost mantle inferred from tri-axial deformation experiments on dry olivine crystals. *Physics of the Earth and Planetary Interiors* 220, 37–49. doi:10.1016/j.pepi.2013.04.008, 2013.
- 545

- Demouchy, S., Tommasi, A., Barou, F., Mainprice, D. and Cordier, P.: Deformation of olivine in torsion under hydrous conditions. *Phys. Earth Planet. Inter.* 202–203, 56–70. doi: 10.1016/j.pepi.2012.05.001, 2012.
- Demouchy, S., Tommasi, A., Ionov, D., Higgie, K. and Carlson, R.W.: Microstructures, Water Contents, and Seismic Properties of the Mantle Lithosphere beneath the Northern limit of the Hangay Dome, Mongolia. *Geochem. Geophys. Geosyst.* 2018GC007931. doi:10.1029/2018GC007931, 2019.
- 550 de Wit, R.: Linear theory of static disclinations. In: *Fundamental aspects of dislocation theory*. In: Simmons, J.A., de Wit, R., Bullough, R. (Eds.), NBS Spec. Publ. 317, vol. 1, pp. 651–680 (National Bureau of Standards, Washington, DC), ISBN: 9781483274928, 1970.
- Djaka, K.S., Villani, A., Taupin, V., Capolungo, L. and Berbenni, S.: Field Dislocation Mechanics for Heterogeneous elastic materials: A numerical spectral approach, *Comput. Methods Appl. Mech. Eng.* 315 921–942, doi:10.1016/j.cma.2016.11.036, 2017.
- 555 Evans, B. and Goetze, C.: The temperature variation of hardness of olivine and its implication for polycrystalline yield stress, *Journal of Geophysical Research*, 84, 5505–5524, 1979.
- Faul, U.: Dislocation structure of deformed olivine single crystals from conventional EBSD maps. *Phys Chem Minerals* 1–15. doi:10.1007/s00269-021-01157-3, 2021.
- 560 Frank, F.C.: I. Liquid crystals. On the theory of liquid crystals. *Discuss. Faraday Soc.* 25, 19. doi: 10.1039/df9582500019, 1958.
- Fressengeas, C. and Beausir, B.: Tangential continuity of the curvature tensor at grain boundaries underpins disclination density determination from spatially mapped orientation data 1–6. doi:10.1016/j.ijsolstr.2018.08.015, 2018.
- 565 Fressengeas, C., Taupin, V. and Capolungo, L.: An elasto-plastic theory of dislocation and disclination fields. *Int. J. Solid. Struct.* 48, 3499–3509. doi:10.1016/j.ijsolstr.2011.09.002, 2011.
- Frey, F.A. and Prinz, M.: Ultramafic inclusions from San Carlos, Arizona: petrologic and geochemical data bearing on their petrogenesis. *Dev. Petrol.* 5, 129–176. http://dx. doi.org/10.1016/B978-0-444-41658-2.50013-4, 1978.
- 570 Friedel, G.: The mesomorphic states of matter. *Ann. Phys.* 18, 273–474. http://dx. doi.org/10.1201/9780203022658.ch1b., 1922.
- Gasc, J., Demouchy, S., Barou, F., Koizumi, S. and Cordier, P.: Creep mechanisms in the lithospheric mantle inferred from deformation of iron-free forsterite aggregates at 900–1200 °C. *Tectonophysics* 761, 16–30. doi:10.1016/j.tecto.2019.04.009, 2019.
- Goetze, C.: The mechanisms of creep in olivine, *Philosophical Transactions of the Royal Society of London A*, 288, 99–119. doi:10.1098/rsta.1978.0011, 1978. <https://www.jstor.org/stable/74978>, 1978.
- 575 Gouriet, K., Cordier, P., Garel, F., Thoraval, C., Demouchy, S., Tommasi, A. and Carrez, P.: Dislocation dynamics modelling of the power-law breakdown in olivine single crystals: Toward a unified creep law for the upper mantle. *Earth Planet. Sci. Lett.* 506, 282–291. doi:10.1016/j.epsl.2018.10.049, 2019.

- Gueguen, Y., and Darot, M.: Microstructure and stresses in Naturally deformed peridotites. *Rock Mechanics suppl.* 9, 159–172. doi: 10.1007/978-3-7091-8588-9_17, 1980.
- 580
- Hansen, L.N., Wallis, D., Breithaupt, T., Thom, C.A. and Kempton, I.: Dislocation Creep of Olivine: Backstress Evolution Controls Transient Creep at High Temperatures. *J. Geophys. Res. Solid Earth* 126, 1–21. doi:10.1029/2020JB021325, 2021.
- Hansen, L.N., Zimmerman, M.E., Dillman, A.M. and Kohlstedt, D.L.: Strain localization in olivine aggregates at high temperature: a laboratory comparison of constant-strain rate and constant-stress boundary conditions. *Earth Planet. Sci. Lett.* 333–334, 134–145. doi:10.1016/j.epsl.2012.04.016, 2012.
- 585
- Heinemann, S., Wirth, R., Gottschalk, M. and Dresen, G.: Synthetic [100] tilt grain boundaries in forsterite: 9.9 to 21.5°. *Phys. Chem. Miner.* 32, 229–240. doi:10.1007/s00269-005-0448-9, 2005.
- Hielscher, R. and Schaeben, H.: A novel pole figure inversion method: specification of the MTEX algorithm. *J. Appl. Cryst.*, 41, 1024–1037, doi:10.1107/S0021889808030112, 2008
- 590
- Hirth, G. and Kohlstedt, D. L., 2003. Rheology of the Upper Mantle and the Mantle Wedge: A View from the Experimentalists in The Subduction Factory, Eiler, J., ed. American Geophysical Union Geophysical Monograph 138, 83-105.
- Hirth, J.P. and Lothe, J.: *Theory of Dislocations* (McGraw-Hill, New York), 1982
- 595
- Hutchinson, J. W.: Creep and plasticity of hexagonal polycrystals as related to single crystal slip. *Metall. Trans. A* 8, 1465–1469, doi: 10.1007/BF02642860, 1977.
- Kleman, M. and Friedel, J.: Disclinations, dislocations, and continuous defects: a reappraisal. *Rev. Mod. Phys.* 80, 61. doi:10.1103/RevModPhys.80.61, 2008.
- 600
- Kohlstedt, D.L., Goetze, C., Durham, W.B. and Vander Sande, J.: New technique for decorating dislocations in olivine. *Science* 191, 1045–1046, doi: 10.1126/science.191.4231.1045, 1976.
- Langdon, T. G.: Grain boundary sliding revisited: developments in sliding over four decades. *J. Mater. Sci.* 41, 597–609, doi:10.1007/s10853-006-6476-0, 2006
- Li, J.C.M.: Disclination model of high angle grain boundaries. *Surface Sci.* 31,12., doi:10.1016/0039-6028(72)90251-8, 1972.
- 605
- Lopez-Sanchez, M.A., Tommasi, A., Ben Ismail, W. and Barou, F.: Dynamic recrystallization by subgrain rotation in olivine revealed by electron backscatter diffraction. *Tectonophysics* 815, 228916. doi:10.1016/j.tecto.2021.228916, 2021
- Mughrabi, H.: On the role of strain gradients and long-range internal stresses in the composite model of crystal plasticity. *Mat. Sci. Eng. A* A317, 171–180, doi:10.1016/S0921-5093(01)01173-X, 2001.
- 610
- Mussi, A., Cordier, P. and Demouchy, S.: Characterization of dislocation interactions in olivine using electron tomography. *Phil. Mag.* 95, 335–345. doi:10.1080/14786435.2014.1000996, 2015.

- Mussi, A., Cordier, P., Demouchy, S. and Vanmansart, C.: Characterization of the glide planes of the [001] screw dislocations in olivine using electron tomography. *Phys Chem Minerals* 41, 537–545. doi:10.1007/s00269-014-0665-1, 2014.
- 615 Miyazaki, T., Sueyoshi, K. and Hiraga, T.: Olivine crystals align during diffusion creep of Earth's upper mantle. *Nature* 502, 321–326. doi:10.1038/nature12570, 2013.
- Paterson, M.S.: Rock deformation experimentation. *Geophys. Monogr.* 56, 187–194, doi:10.1029/GM056p0187, 1990.
- Paterson, M.S. and Olgaard, D.L.: Rock deformation tests to large shear strains in torsion. *J. Struct. Geol.* 22, 1341–1358. , doi:10.1016/S0191-814(00)00042-0, 2000.
- 620 Raleigh, C.B.: Mechanism of plastic deformation of olivine. *J. Geophys. Res.* 73, 5391–5406, doi:10.1029/JB073i016p05391, 1968.
- Read, W.T. and Shockley, W.: Dislocation models of crystal grain boundaries. *Phys. Rev. Materials* 78, 275–289. doi: 10.1103/PhysRev.78.275, 1950.
- Romanov, A.E. and Kolesnikova, A.L.: Application of disclination concept to solid structures. *Progress in Materials Science* {54}, {740–769}. doi:10.1016/j.pmatsci.2009.03.002, 2009.
- 625 Romanov, A.E. and Vladimirov, V.I., 1992. Disclinations in crystalline solids. In: Nabarro, F.R.N. (Ed.), *Dislocations in Solids*, vol. 9. Elsevier, Amsterdam, p. 191.
- Romanov, A.E., Kolesnikova, A.L., 2009. Application of disclination concept to solid structures. *Prog. Mat. Sci.* 54, 740.
- 630 Samae, V., Cordier, P., Demouchy, S., Bollinger, C., Gasc, J., Koizumi, S., Mussi, A., Schryvers, D. and Idrissi, H.: Stress-induced amorphization triggers deformation in the lithospheric mantle. *Nature* 1–16. doi:10.1038/s41586-021-03238-3, 2021.
- Sun, X.-Y., Cordier, P., Taupin, V., Fressengeas, C. and Jahn, S.: Continuous description of a grain boundary in forsterite from atomic scale simulations: the role of disclinations. *Phil. Mag.* 96, 1757–1772. doi:10.1080/14786435.2016.1177232, 2016.
- 635 Sun, X.Y., Fressengeas, C., Taupin, V., Cordier, P. and Combe, N.: Disconnections, dislocations and generalized disclinations in grain boundary ledges. *International Journal of Plasticity* 104, 134–146. doi:10.1016/j.ijplas.2018.02.003, 2018.
- Sutton, A.P. and Vitek, V.: On the structure of tilt grain boundaries in cubic metals. I. Symmetrical tilt boundaries. *Phil. Trans. Roy. Soc. London A309*, 1, doi: 10.1098/rsta.1983.0020, 1983.
- 640 Taupin, V., Capolungo, L. and Fressengeas, C.: Disclination mediated plasticity in shear-coupled boundary. *Int. J. Plast.* 53, 179–192, doi: 10.1016/j.ijplas.2023.08002, 2014.
- Thieme, M., Demouchy, S., Mainprice, D., Barou, F. and Cordier, P.: Stress evolution and associated microstructure during transient creep of olivine at 1000–1200 °C. *Physics of the Earth and Planetary Interiors* 278, 34–46. doi:10.1016/j.pepi.2018.03.002, 2018.
- 645

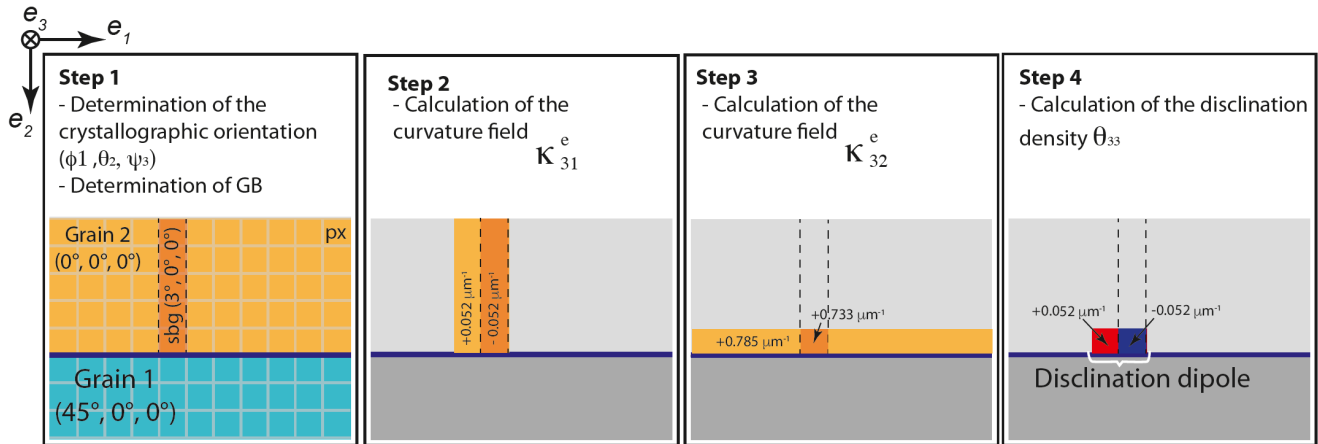
- Tommasi, A. and Vauchez, A.: Heterogeneity and anisotropy in the lithospheric mantle. *Tectonophysics* 661, 11–37. doi:10.1016/j.tecto.2015.07.026, 2015.
- Upadhyay, M., Capolungo, L., Taupin, V. and Fressengeas, C.: Grain boundary and triple junction energies in crystalline media: A disclination based approach. *Int. J. Solid. Struct.*, 48, 3176–3193. doi:10.1016/j.ijsolstr.2011.07.009, 2011.
- 650 Volterra, V.: Sur l'équilibre des corps élastiques multiples connexes. *Ann. Sci. Ecol. Norm. Sup.* III 24, 401–517, doi: 10.24033/asens.583, 1907.
- Von Mises, R.: Mechanik der plastischen Formänderung von Kristallen. *Z. Angew. Math. Mech.* 8, 161–185, doi: [10.1002/zamm.19280080302](https://doi.org/10.1002/zamm.19280080302), 1928.
- Wallis, D., Hansen, L.N., Britton, B. T. and Wilkinson, A.J.: Geometrically necessary dislocation densities in olivine
655 obtained using high-angular resolution electron backscatter diffraction 1–38. doi:10.1016/j.ultramic.2016.06.002, 2016.
- Wallis, D., Hansen, L.N., Britton, T.B. and Wilkinson, A.J.: Dislocation Interactions in Olivine Revealed by HR-EBSD 122, 1–20. doi:10.1002/2017JB014513, 2017.
- Wallis, D., Sep M. and Hansen, L.N.: Transient creep in subduction zones by long-range dislocation interaction in olivine. *J. Geophys. Res.* 127, Issue 1, e2021JB022618, doi: 10.1029/2021JB022618, 2022.
- 660 Wang, N., Chen, Y., Wu, G., Zhao, Q., Zhang, Z., Zhu, L. and Luo, J.: Non-equivalence contribution of geometrically necessary dislocation and statistically stored dislocation in work-hardened metals. *Materials Science & Engineering A* 836, 142728. doi:10.1016/j.msea.2022.142728, 2022.
- Warren, J.M. and Hirth, G.: Grain size sensitive deformation mechanisms in naturally deformed peridotites, *Earth Planet. Sci. Lett.*, 248, 423–435, doi: 10.1016/J.epsl.2006.06.006, 2006.
- 665 Zimmerman, M.E. and Kohlsreidt, D.L.: Rheological Properties of Partially Molten Lherzolite. *J. Petrol.* 45, 275–298. doi:10.1093/petrology/egg089, 2004.
- Zoller, K., Kalácska, S., Ispánovity, P.D. and Schulz, K.: Microstructure evolution of compressed micropillars investigated by in situ HR-EBSD analysis and dislocation density simulations. *Comptes Rendus. Physique* 22, 267–293. doi:10.5802/crphys.55, 2021.

670

675

680

685

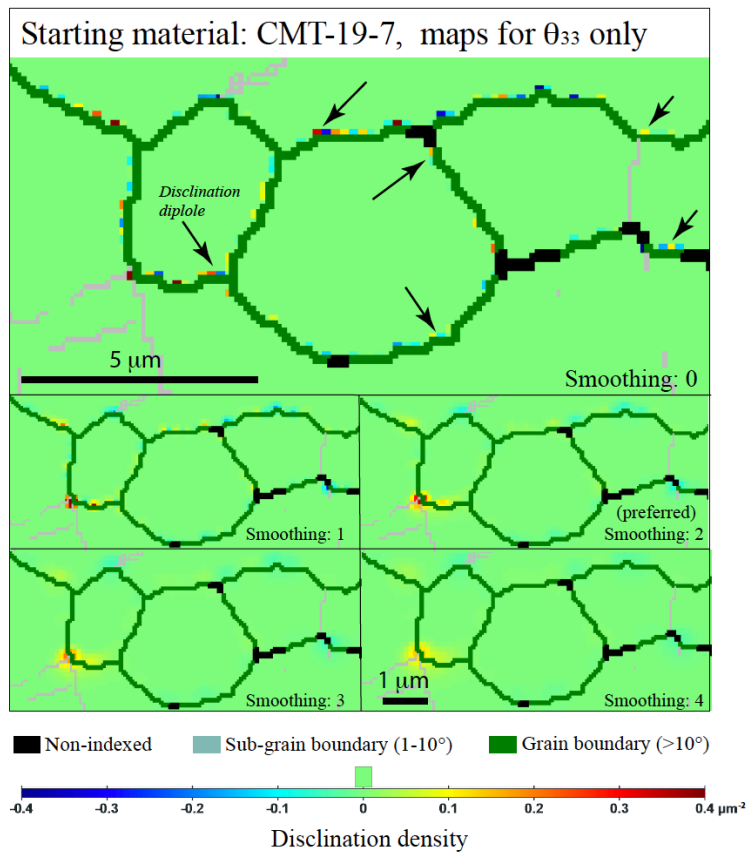


690

695

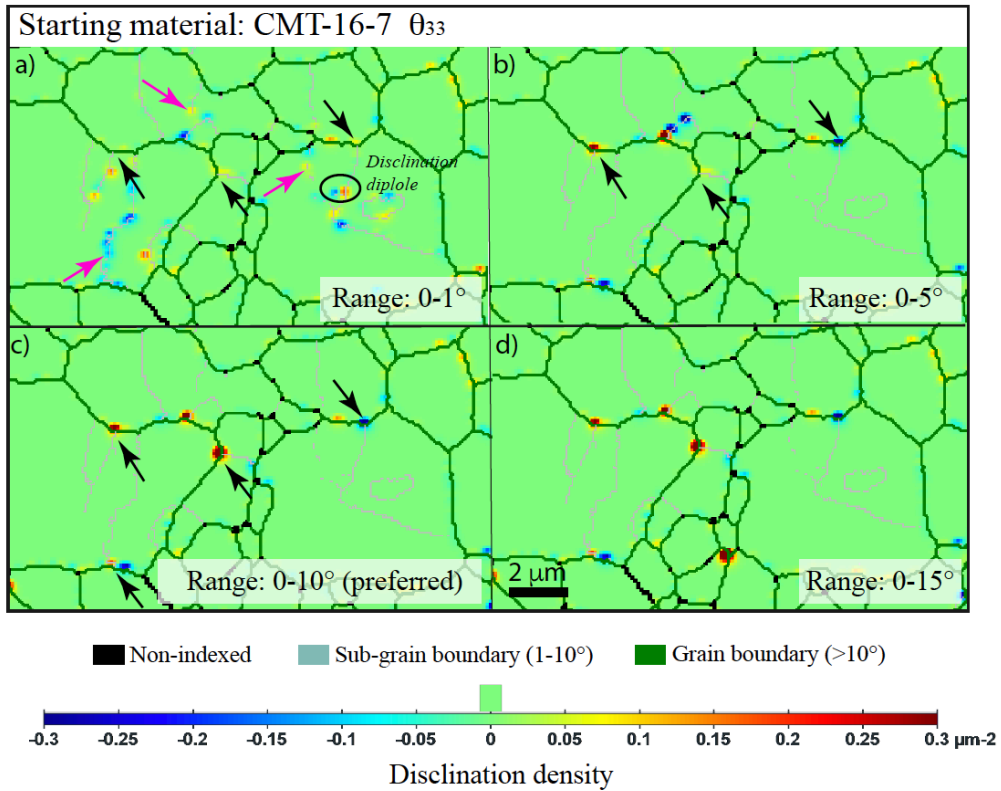
Figure 1: Sketch illustrating an example of calculation of the wedge disclination θ_{33} along a grain boundary. (a) Two grains with orientations given by Euler angles (grain 1) $45^\circ, 0^\circ, 0^\circ$ and (grain 2) $0^\circ, 0^\circ, 0^\circ$, which define a pure tilt grain boundary of misorientation $> 5^\circ$. A subgrain is inserted within grain 2 with a disorientation of 3° around axis e_3 ; (b) the field of K_{31}^e component of the curvature tensor is derived by one-sided differentiation of field of ω_3^e component of the elastic rotation vector; (c) the field of K_{32}^e component of the curvature tensor is derived by forward differentiation of ω_3^e ; (d) The density of wedge disclinations θ_{33} is derived from forward differentiation of the field of K_{31}^e and K_{32}^e components of the curvature tensor. Redrawn after Fressengeas & Beausir (2018, their Figure 2). NB: densities are here not yet normalized by the step size, see main text for details.

700



705 **Figure 2 Comparison of wedge disclination densities θ_{33} with different smoothing factors of 0, 1, 2, 3 and 4, for selected area (top**
left corner) of the starting material map (sample CMT16-7). A user-defined scale was used here; the step size was 0.1 μm and
disorientation for disclination detection was 0-10°.

710



715

Figure 3 Comparison of wedge disclination densities θ_{33} with different range of disorientation for disclination detection for selected area (left edge) of the starting material map (sample CMT16-7). A user-defined scale was used here; the step size was 0.1 μm and smoothing factor=2. Black arrows indicate disclination at triple junctions or grain boundary/sub-grain boundaries junctions and the pink arrows indicate disclination at the intragranular tip of sub-grain boundaries.

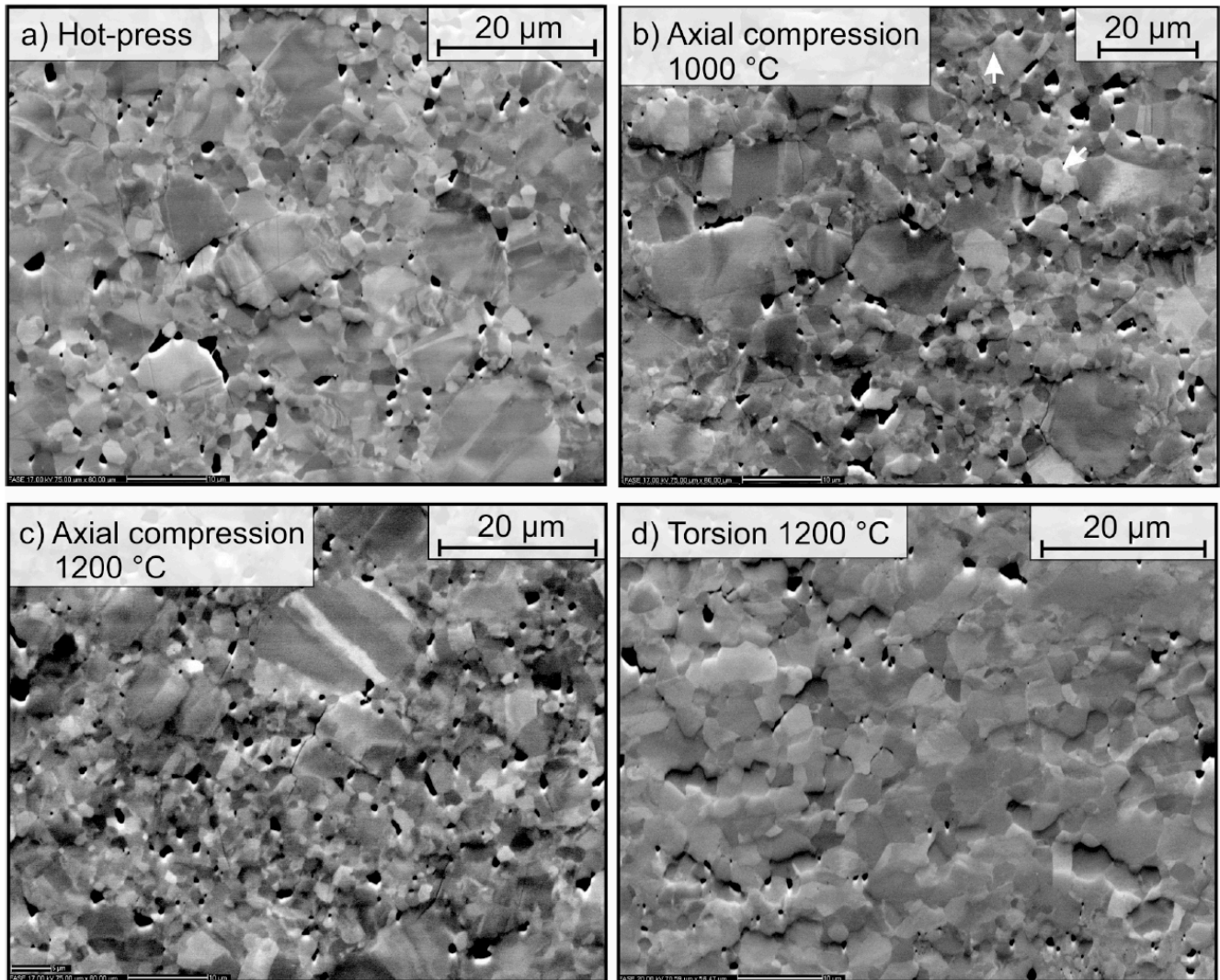
720

725

730

735

740

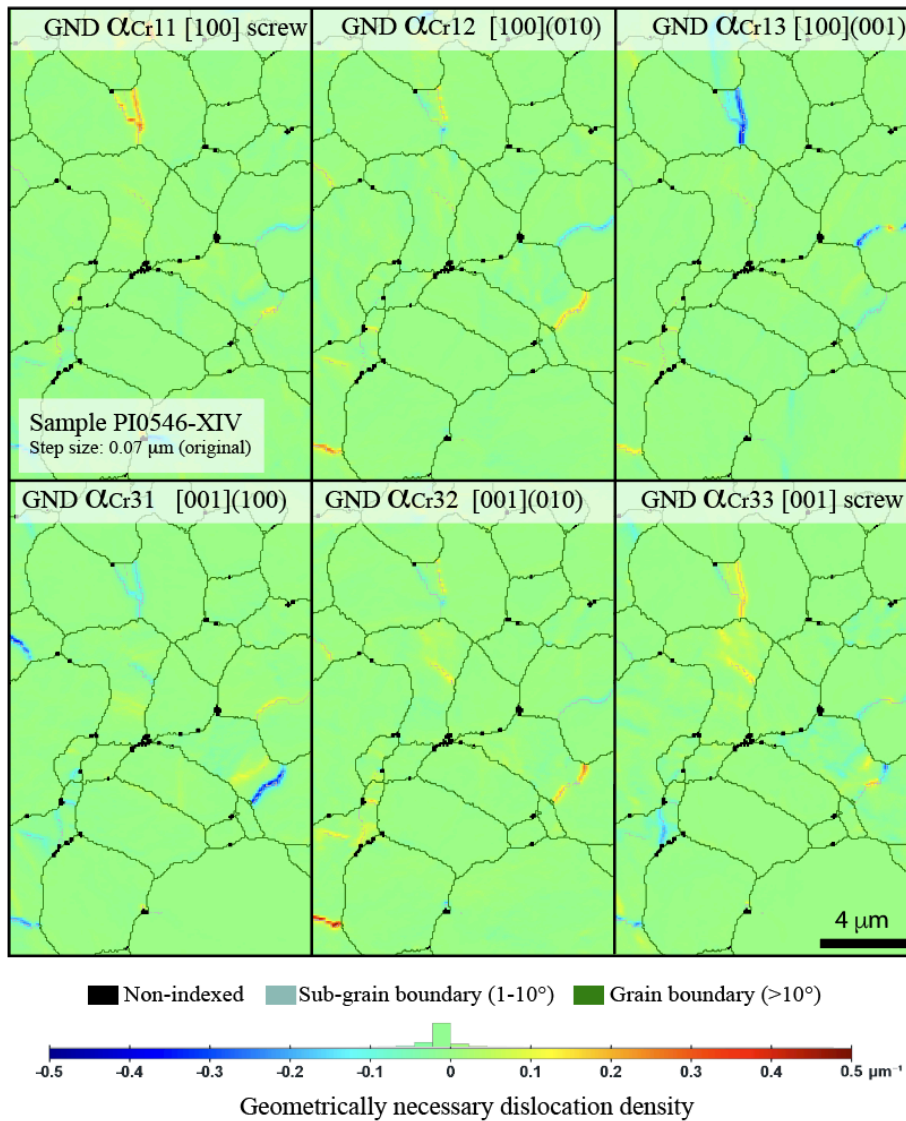


745 **Figure 4** Forward scattered electron images from scanning electron microscopy (SEM). (a) typical image from starting material, undeformed but sintered aggregate by hot-pressing at high temperature and pressure (sample CMT16-7); (b) after axial compression at 1000 °C and for 7.3 % of finite strain (CMT17-2); (c) after axial compression at 1200 °C and for 8.6 % of finite strain (CMT16-9); (d) after torsion at 1200 °C and for 2.05 % of equivalent strain (PI0546). Dark areas are plug outs from polishing and residual pores from hot-press step, see main text for details.

750

755

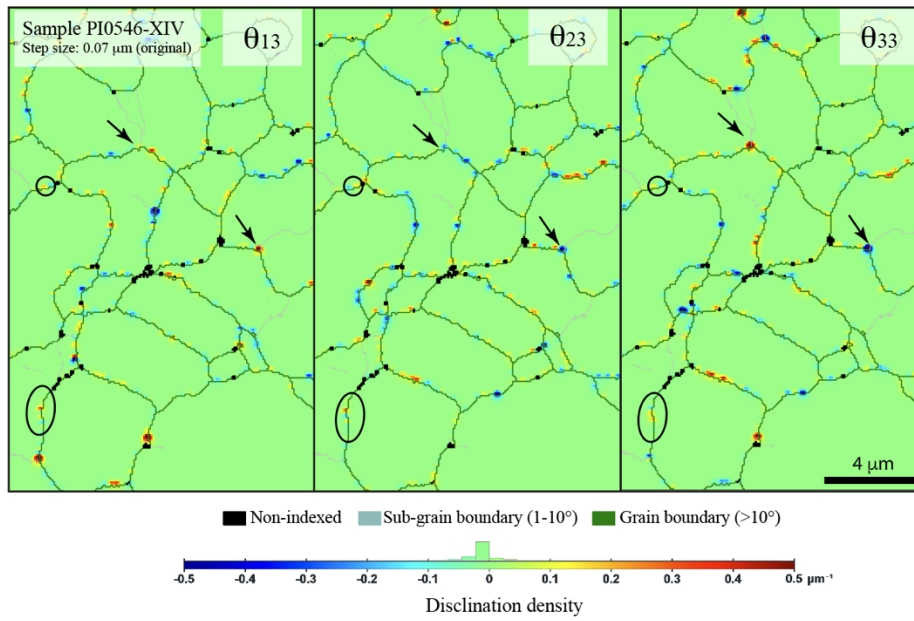
760



765 **Figure 5** Representative distribution of the different GND reported in the crystallographic frame in the sample deformed in
 766 torsion (PI0546-XIV). The density scale is automatically set up for this set of maps; the step size was 0.07 μm (original acquisition
 767 step size) and smoothing factor=2 was used.

770

775



780 **Figure 6** Representative distribution of the different disclinations (θ_{13} , θ_{23} , and θ_{33}) reported in a sample deformed in torsion
 (PI0546-XIV). The density scale is user-defined for this set of maps; the step size was 0.07 μm and a smoothing factor=2 was used.

785

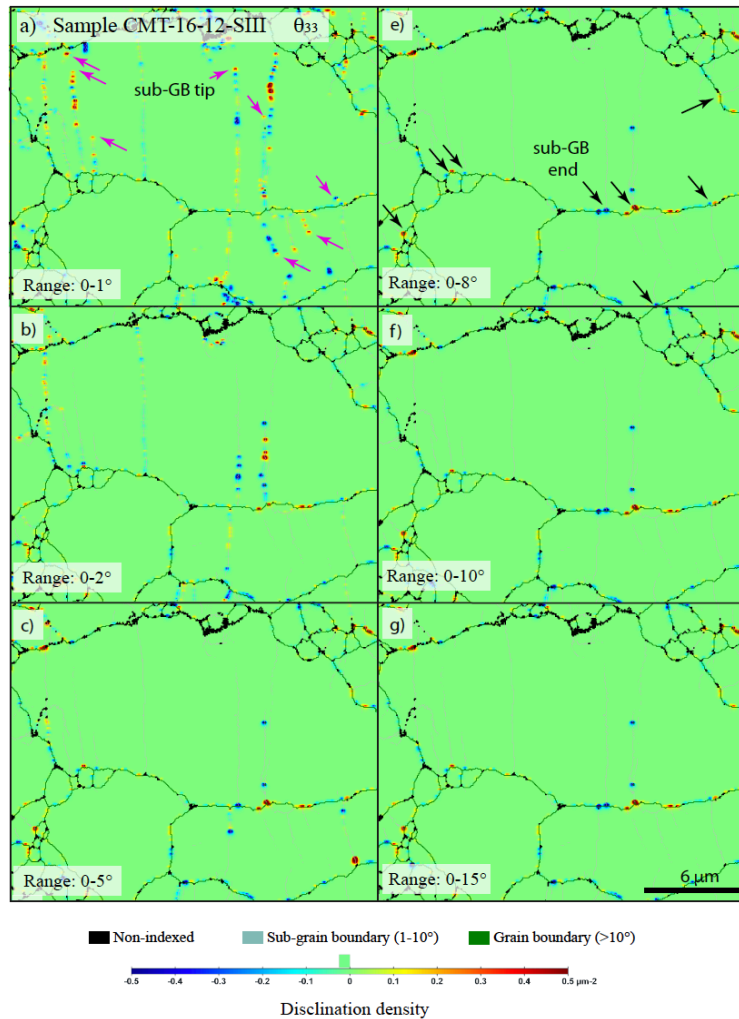
790

795

800

805

810

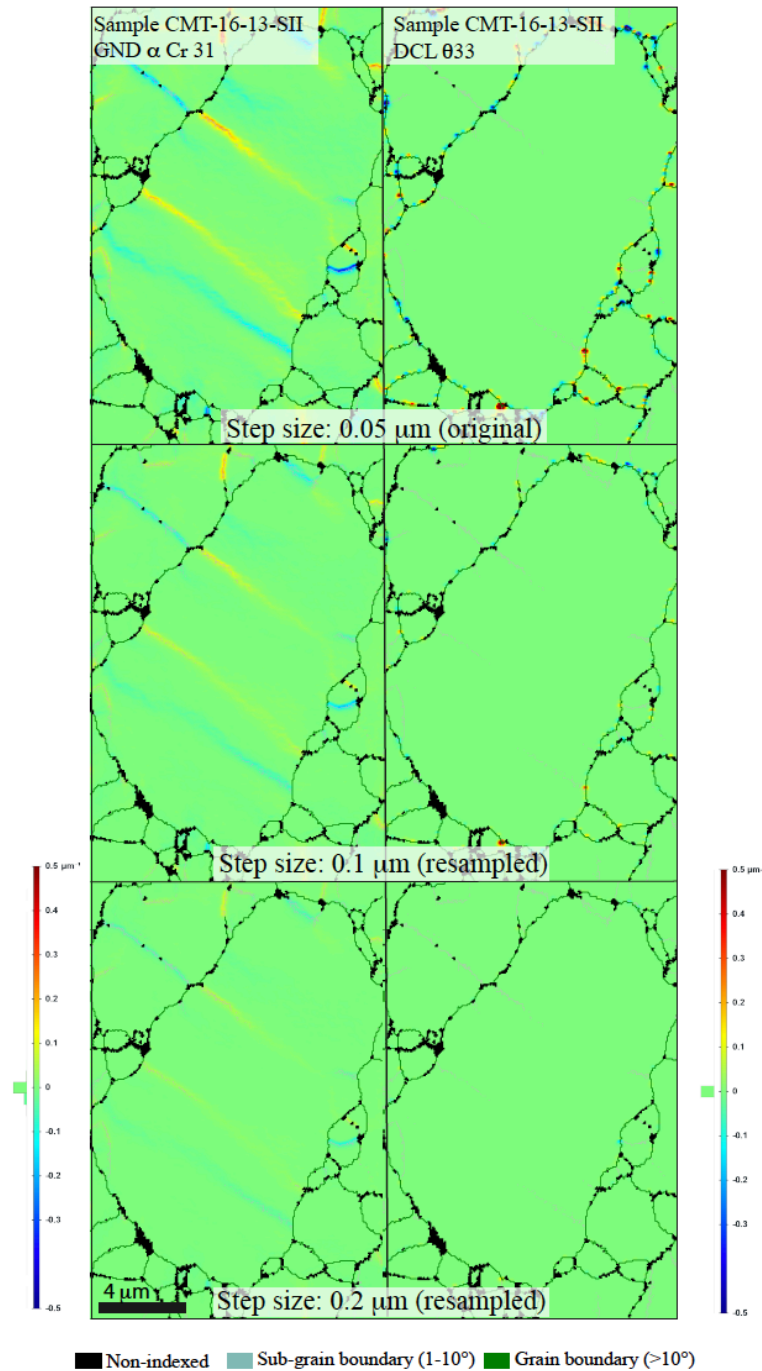


815 **Figure 7** Comparison of wedge disclination densities θ_{33} with different range of disorientation for the full EBSD map from a
sampled deformed in axial compression (sample CMT16-12, 1200 °C, low strain ~1%) centered on a large olivine grain. A user-
defined scale was used here; the step size was 0.06 μm and smoothing factor=2. Black arrows indicate disclination at triple
junctions or grain boundary/sub-grain boundaries junctions, and the pink arrows indicate disclination at the intragranular tip of
sub-grain boundaries.

820

825

830

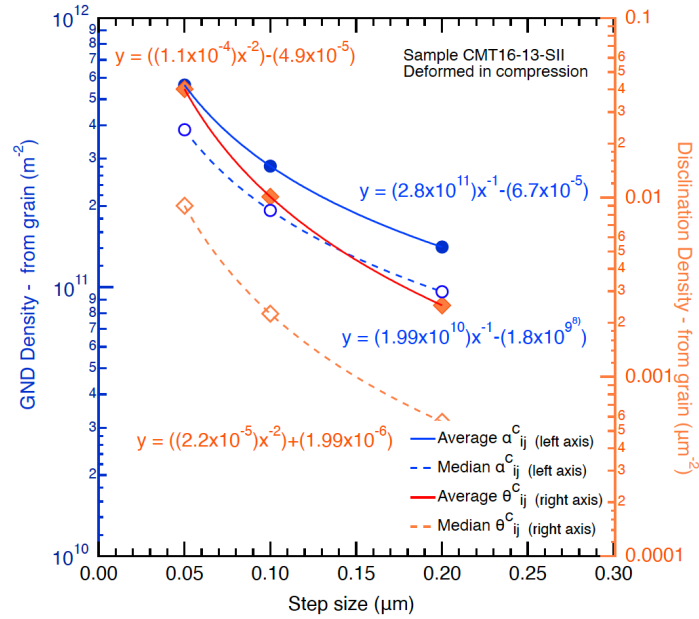


835

Figure 8 Representative distribution of GND (α'_{31}) and disclinations (θ_{33}) for different values of step size: 0.05 μm (original step size), 0.1 μm (new sampling) and 0.2 μm (new sampling) in a sample deformed in axial compression (CMT16-13-SII, 1200 °C, low strain ~3.7%) centered on a large olivine grain. The density scale is user-defined and the same for this set of maps; for both GND and disclinations a smoothing factor=2 was used.

840

845



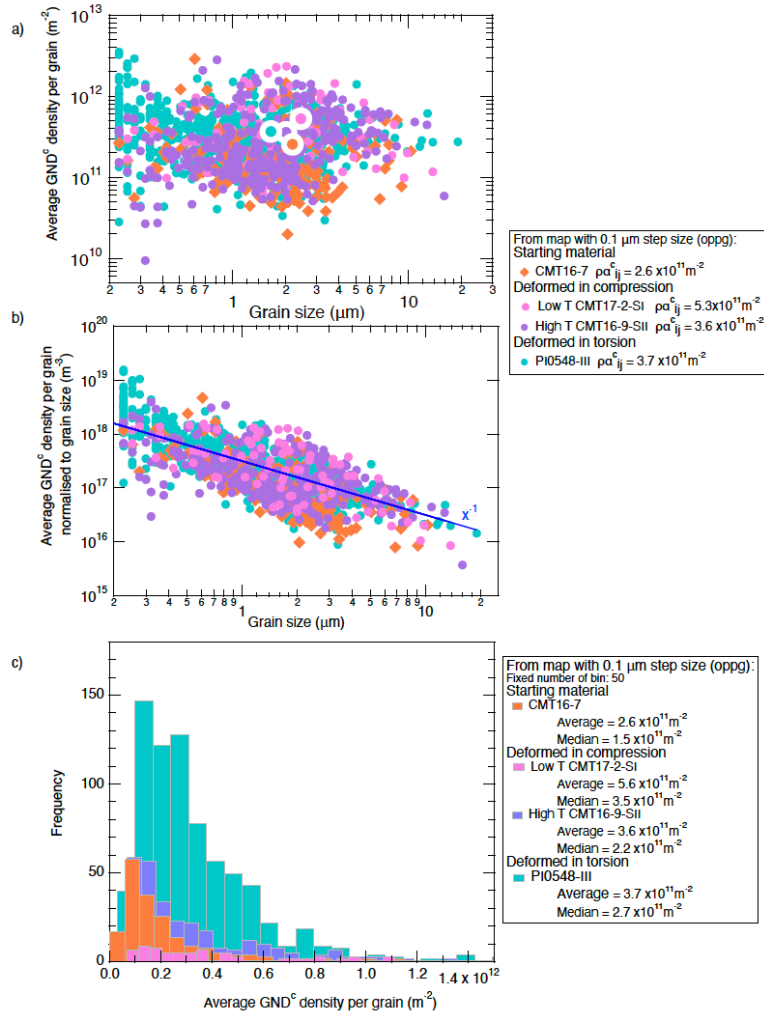
850 Figure 9 Resulting variation of average and median oppg GND and disclination densities as a function of the EBSD acquisition
855 step size from 0.05 μm (original step size), to 0.1 μm (new sampling) and 0.2 μm (as displayed in Figure 8).

855

860

865

Figure 10 - Demouchy et al.

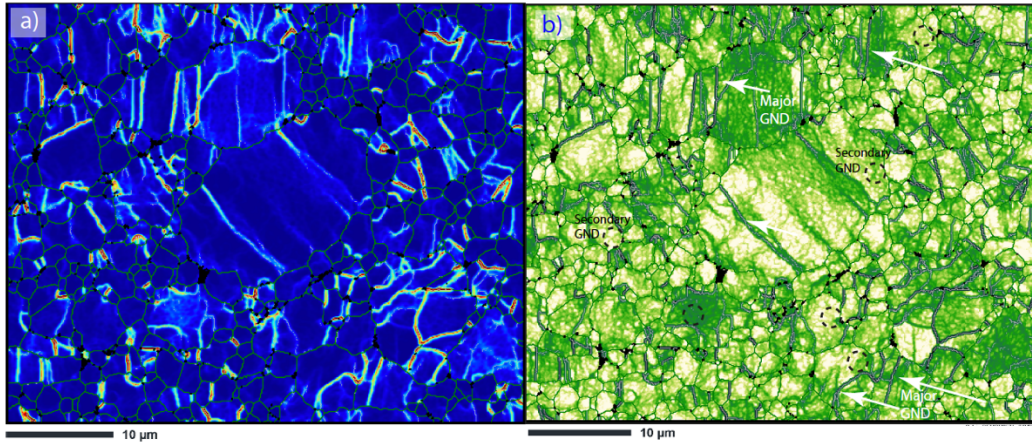


870

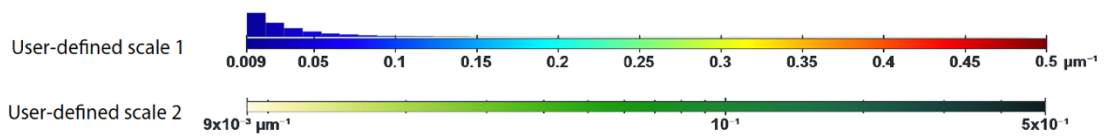
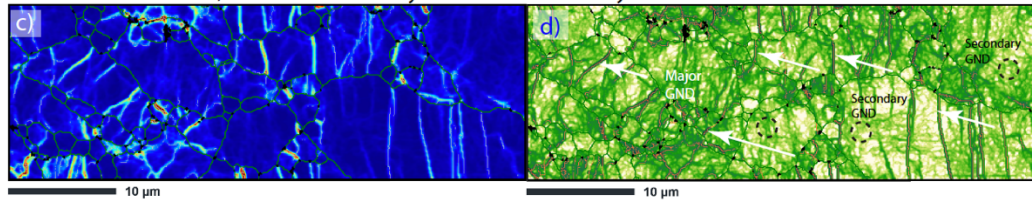
Figure 10 (a) Representative distribution of oppg GND density as a function of the grain size in the starting material (CMT16-7), in two samples deformed in axial compression (low temperature CMT17-2 and at high temperature CMT16-9-SII) and in a sample deformed in torsion (PI0546-III). The step size was 0.1 μm (original acquisition step size). Also shown is the average oppg GND density for each sample as a large symbol; (b) Same samples as in (a), but with density normalized to the grain size. It permits to identify a bias, small grains have more GND than large grain since the GND distribution is particularly heterogenous in large grain with the formation of subgrain boundaries, The dash dark blue line is a guide for the eye with $y=x^{-1}$; (c) same samples as in (a), distribution of oppg GND density as histogram, showing a distribution close to log normal and thus the relative validity of the median of the distribution as compared to the average of the distribution.

875

CMT16-9-SII 1200 °C, 8.6 % strain - Entrywise norm of the Nye tensor



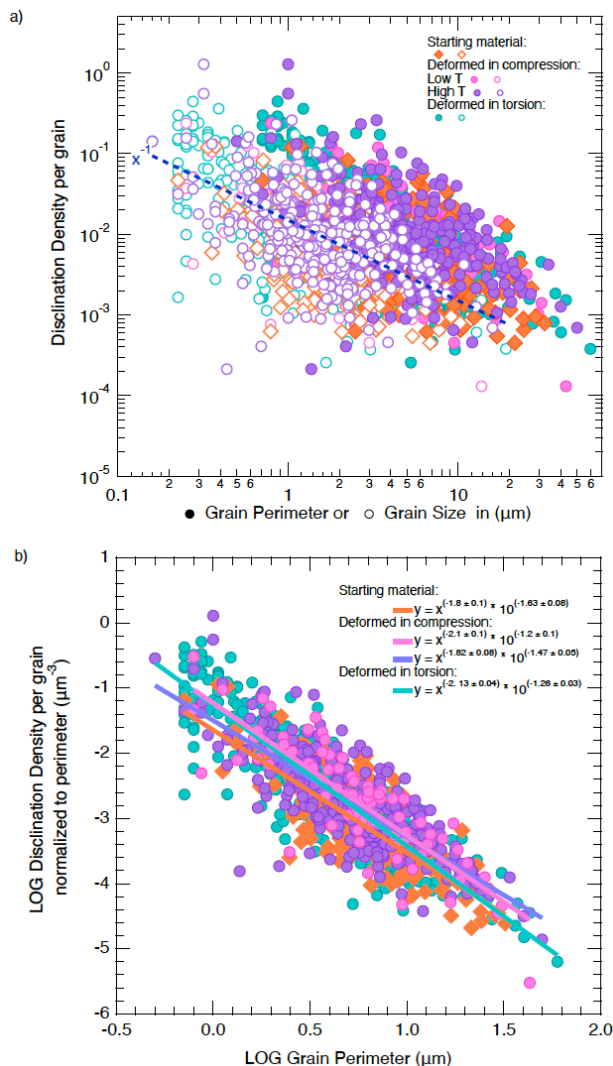
CMT17-2-SI 1000 °C, 7.3 % strain - Entrywise norm of the Nye tensor



880

885

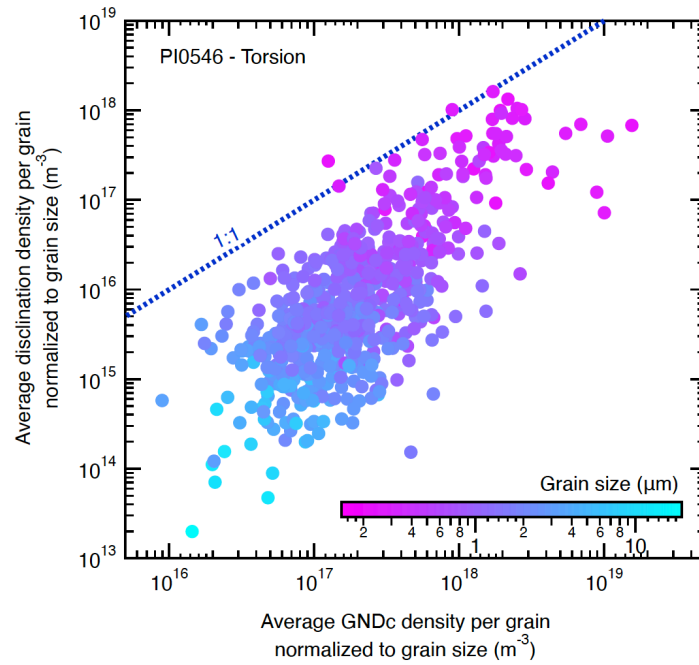
Figure 11 Representative distribution of the different entrywise norm of GND (major and minor, see main text for details) with two different display strategy. (a) and (b) from a sample deformed in compression at high temperature and low stress (CMT16-9) and (c) and (d) at low temperature and high stress (CMT17-2). In (a) and (c), the jet color scale was used with a is linear user-defined scale and a smoothing factor=2; in (b) and (d) the ‘linear green’ color scale was used with a is log user-defined log scale and a smoothing factor=1. The step size was 0.1 μm .



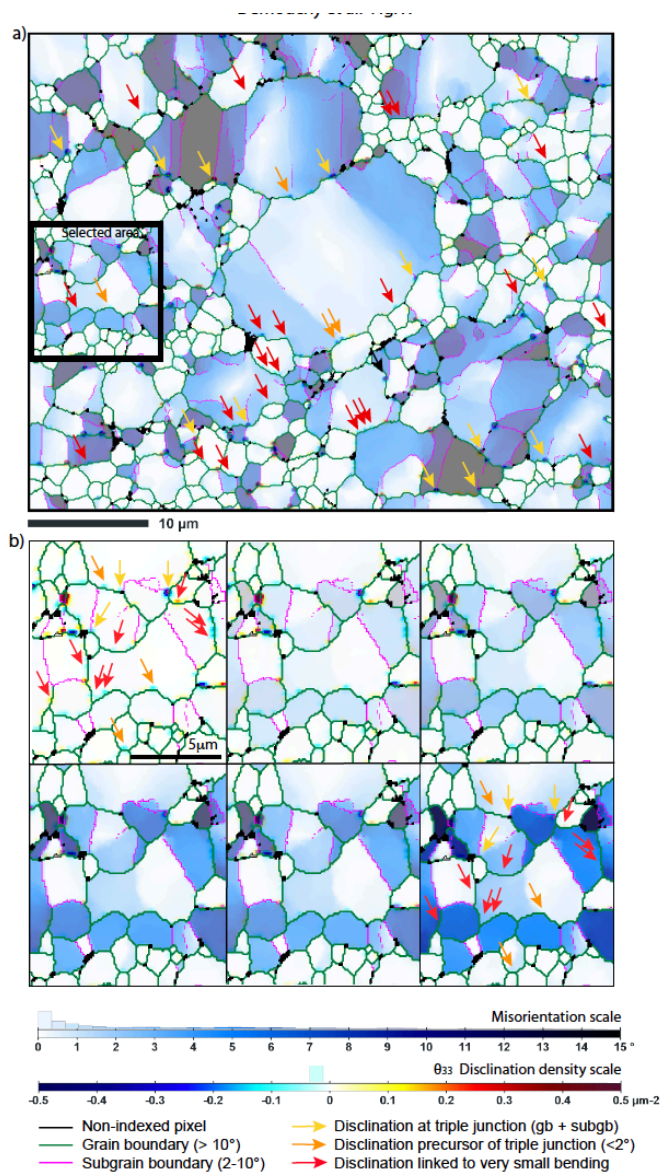
890

Figure 12 (a) Distribution of oppg disclination densities as a function of the grain size (hollow symbol) or grain perimeter (full symbol) in the starting material (CMT16-7), in two samples deformed in axial compression (low temperature CMT17-2 and at high temperature CMT16-9-SII) and in a sample deformed in torsion (PI0546-III). The step size was $0.1 \mu\text{m}$ (original acquisition step size). The dash dark blue line is a guide for the eye with a $y=x^{-1}$ function. (b) Distribution of oppg disclination densities normalized to the grain perimeter, as a function of the grain perimeter in the starting material (CMT16-7), in two samples deformed in axial compression (low temperature CMT17-2 and at high temperature CMT16-9-SII) and in a sample deformed in torsion compression (PI0546-III). Also shown is the least-squared fit through each sample data set and the equation of the fit. See main text for details. The step size was $0.1 \mu\text{m}$ (original acquisition step size).

900



905 **Figure 13. Distribution of oppg disclination densities normalized to the grain size as a function of the oppg GND density normalized to the grains size for sample PI0546-III. The data points are color coded according to the associated grain size. The step size was $0.1 \mu\text{m}$ (original acquisition step size). The dash dark blue line is a guide for the eye with 1:1 slope.**

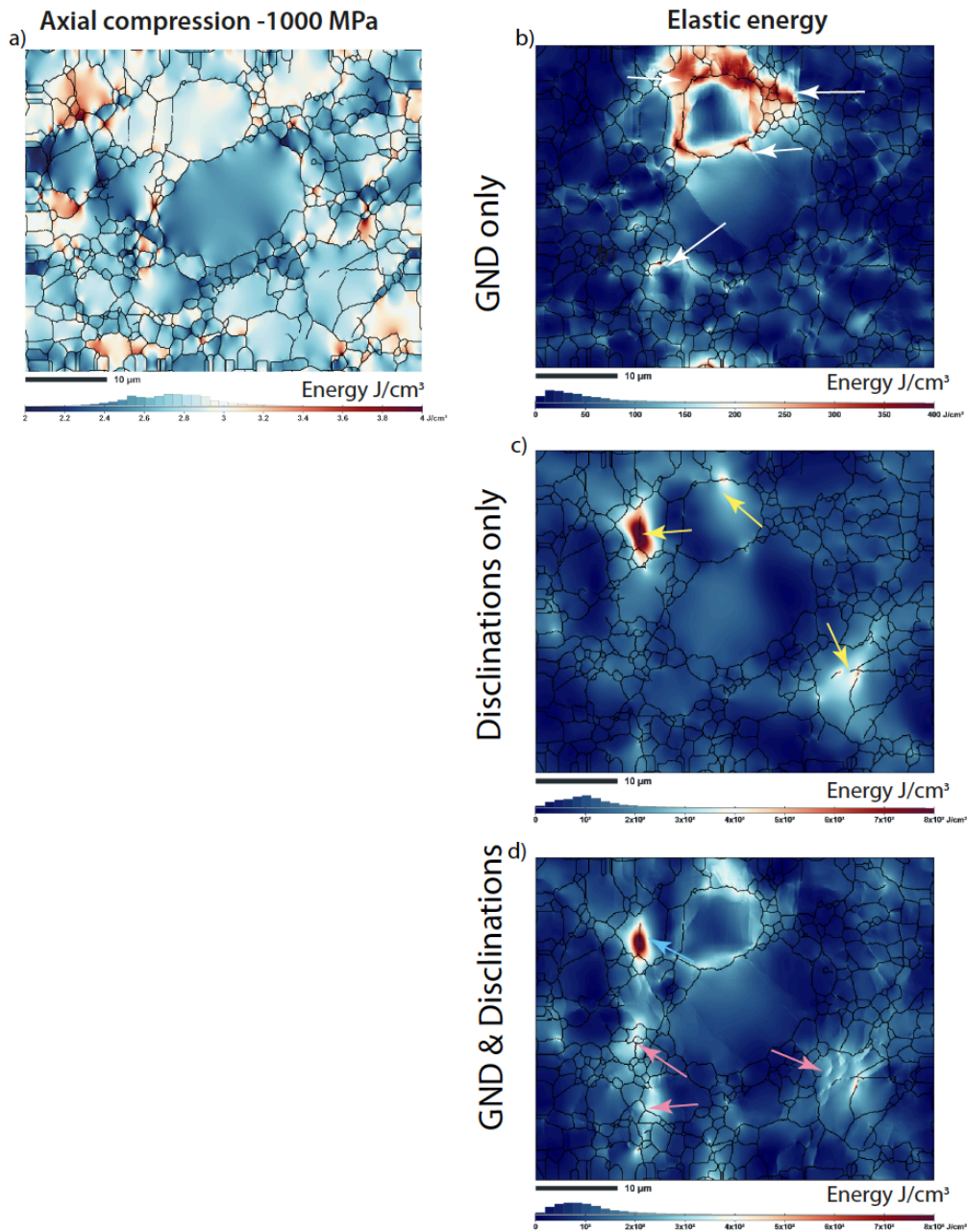


910

Figure 14 (a) Misorientation maps in sample CMT16-9 (extracted in the full map) surimposed on the disclination density map (θ_{33} only). Misorientation in each grain is relative to gravity center. (b) further enlargement of the map in Fig. 14a but for different levels of overlay to show the relationship between misorientation from GND and misorientation from disclinations. Three populations of disclinations are identified (yellow, orange and red arrows). See main text for details.

915

920



925 **Figure 15** Maps resulting from field dislocation and disclination mechanics (FDDM) simulations of a section of sample CMT16-9 (a) after axial compression (1000 MPa), designed to reveal mechanical incompatibilities from crystallographic orientation in adjacent olivine grains; (b) with no compression, designed to reveal the action of GND only on internal elastic energy; (c) or disclination only on internal elastic energy; or (d) both GND and disclination on internal elastic energy.

930

Tables and table captions

940 **Table 1** Experimental parameters and mechanical results for the selected deformation experiments investigated by EBSD in this study. Original deformation curves (stress-strain) are reported in Demouchy et al. (2012) and Thieme et al., (2018). Uncertainties on T are up to ± 2 °C, 20 MPa for stress, and negligible for strain and strain rate (<1%). NB: * denotes an EBSD map centered on a relatively large grain, thus with a low number of grains.

Sample	Temperature T (°C)	Finite strain ε/γ (%)	Equivalent strain rate $\dot{\varepsilon}/\dot{\gamma}$ (s ⁻¹)	Diff. stress σ (MPa)
<i>Starting material (hot-pressed)</i>				
CMT16-7 SII	1200	0	0	0
<i>Deformation in axial compression</i>				
CMT16-6 SIII	1000	0.11	1.9×10^{-6}	80
CMT16-8 SV	1000	1.07	3.3×10^{-6}	684
CMT16-8 SVI	1000	1.07	3.3×10^{-6}	684
CMT17-2 SI	1000	7.3	1.1×10^{-5}	1073
CMT16-12 SIII*	1200	0.88	7.2×10^{-6}	150
CMT16-13 SII*	1200	3.68	1.0×10^{-5}	313
CMT16-13 SIII	1200	3.68	1.0×10^{-5}	313
CMT16-13 SIV	1200	3.68	1.0×10^{-5}	313
CMT16-9 SII	1200	8.59	1.0×10^{-5}	322
<i>Deformation in torsion</i>				
PI0546 III	1200	1.79	3.6×10^{-5}	248
PI0546 VII	1200	1.79	3.6×10^{-5}	264
PI0546 XVII	1200	1.79	3.6×10^{-5}	264
PI0546 V	1200	2.05	4.1×10^{-5}	264
PI0546 VIII	1200	2.05	4.1×10^{-5}	264
PI0546 XVI	1200	2.05	4.1×10^{-5}	264
PI0546 IX	1200	2.31	4.6×10^{-5}	264
PI0546 XIV*	1200	2.31	4.6×10^{-5}	264
PI0546 XVIII	1200	2.31	4.6×10^{-5}	264

Table 2 For the studied EBSD maps, we report the indexation rate after data treatment, the original step size and subsequent re-step size (*italicized*), the number of detected grains, the average grain size, the calculated partial GND dislocation densities. We provide the average of grain density and the median grain density for α_{ij} . The average for each α_{ij} and θ_{ij} per grain are given in supplementary material in Table S1. Roman numbers identify individual EBSD maps acquired on the same sample ('S' stand for small area maps). Average grain sizes are calculated as the diameter of a circle with equivalent area. Maps from samples deformed in torsion are taken at three different positions and hence with increasing strains.

Sample	Indexation rate (%)	Step size (μm)	Nb. grains	Av. grain size (μm) [§]	$\rho\alpha_{ij}^c$ Average GND density (m^{-2})	$M\alpha_{ij}^c$ Median GND density (m^{-2})	$\rho\theta_{ij}$ - Average Disclination density ($\text{rad}.\mu\text{m}^{-2}$)	$M\theta_{ij}$ - Median Disclination density ($\text{rad}.\mu\text{m}^{-2}$)
<i>Starting material (hot-pressed)</i>								
CMT16-7 SII	97.2	0.1	231	2.038	2.56×10^{11}	1.47×10^{11}	9.82×10^{-3}	$4.08.\times 10^{-3}$
<i>Deformation in axial compression</i>								
CMT16-6 SIII	96.1	0.1	385	1.621	4.84×10^{11}	2.88×10^{11}	3.33×10^{-2}	1.22×10^{-2}
CMT16-8 SV	95.8	0.1	120	2.088	4.05×10^{11}	2.46×10^{11}	1.54×10^{-2}	$6.42.\times 10^{-3}$
CMT16-8 SVI	95.9	0.07	105	1.792	3.28×10^{11}	2.69×10^{11}	2.52×10^{-2}	$8.67.\times 10^{-3}$
		<i>0.1</i>	<i>id.</i>	<i>id.</i>	2.30×10^{11}	1.89×10^{11}	1.77×10^{-2}	$6.07.\times 10^{-3}$
CMT17-2 SI		0.1	82	2.44	5.28×10^{11}	3.55×10^{11}	2.24×10^{-2}	$1.11.\times 10^{-2}$
CMT16-12 SIII*	96.4	0.06	48	1.762	4.50×10^{11}	3.49×10^{11}	6.51×10^{-2}	$8.58.\times 10^{-3}$
		<i>0.1</i>	<i>id.</i>	<i>id.</i>	2.71×10^{11}	2.10×10^{11}	3.99×10^{-2}	$6.28.\times 10^{-3}$
CMT16-13 SII*	94.9	0.05	45	1.376	5.64×10^{11}	3.85×10^{11}	4.02×10^{-2}	9.01×10^{-3}
		<i>0.1</i>	<i>id.</i>	<i>id.</i>	2.82×10^{11}	1.93×10^{11}	1.01×10^{-2}	$2.25.\times 10^{-3}$
		<i>0.2</i>	<i>id.</i>	<i>id.</i>	1.41×10^{11}	9.63×10^{10}	2.51×10^{-3}	5.63×10^{-4}
CMT16-13 SIII	96.1	0.1	298	1.651	4.16×10^{11}	2.76×10^{11}	2.95×10^{-2}	1.17×10^{-2}
CMT16-13 SIV	95.6	0.1	121	1.744	3.89×10^{11}	2.81×10^{11}	2.61×10^{-2}	9.56×10^{-3}
CMT16-9 SII	97.2	0.1	315	2.008	3.58×10^{11}	2.23×10^{11}	2.25×10^{-2}	$7.54.\times 10^{-3}$
<i>Deformation in torsion</i>								
PI0546 III	90.9	0.1	772	1.648	3.67×10^{11}	2.73×10^{11}	2.00×10^{-2}	7.12×10^{-3}
PI0546 VII	95.9	0.1	285	2.1	3.45×10^{11}	2.54×10^{11}	1.86×10^{-2}	7.37×10^{-3}
PI0546 XVII	97.4	0.07	179	2.16	3.33×10^{11}	2.57×10^{11}	3.35×10^{-2}	9.64×10^{-3}
		<i>0.1</i>	<i>id.</i>	<i>id.</i>	2.25×10^{11}	1.83×10^{11}	1.64×10^{-2}	2.47×10^{-3}
PI0546 V	94.9	0.062	189	2.003	3.93×10^{11}	2.64×10^{11}	1.96×10^{-2}	6.92×10^{-3}
		<i>0.1</i>	<i>id.</i>	<i>id.</i>	2.37×10^{11}	1.50×10^{11}	7.53×10^{-3}	2.66×10^{-3}
PI0546 VIII	96.8	0.1	276	2.672	3.05×10^{11}	2.28×10^{11}	1.47×10^{-2}	5.18×10^{-3}
PI0546 XVI	97.6	0.07	185	1.895	3.37×10^{11}	2.40×10^{11}	2.69×10^{-2}	5.98×10^{-3}
		<i>0.1</i>	<i>id.</i>	<i>id.</i>	2.35×10^{11}	1.61×10^{11}	1.32×10^{-2}	2.93×10^{-3}
PI0546 IX	97.1	0.1	277	2.395	2.88×10^{11}	2.25×10^{11}	1.25×10^{-2}	5.45×10^{-3}
PI0546 XIV*	95.9	0.07	42	2.098	3.65×10^{11}	2.64×10^{11}	3.89×10^{-2}	4.73×10^{-3}
		<i>0.1</i>	<i>id.</i>	<i>id.</i>	2.55×10^{11}	1.85×10^{11}	1.91×10^{-2}	2.32×10^{-3}

PI0546 XVIII	97.9	0.07	170	2.566	3.78×10^{11}	2.02×10^{11}	1.92×10^{-2}	4.46×10^{-3}
		<i>0.1</i>	<i>id.</i>	<i>id.</i>	2.64×10^{11}	1.41×10^{11}	9.41×10^{-3}	2.19×10^{-3}

Table 3. Dislocation type, corresponding slip systems and GND in the crystallographic frame (α^c_{ij}).

960

Dislocation type	Main slip systems in olivine	GND notation
Screw	[100]	α^c_{11}
Edge	[100](010)	α^c_{12}
Edge	[100](001)	α^c_{13}
Edge	[001](100)	α^c_{31}
Edge	[001](010)	α^c_{32}
Screw	[001]	α^c_{33}

965

970

975

980

985

990

Supplementary Online Material:

995

Supplementary Excel file with Table S1: Compilation of the average oppg α_{ij}^c , $\rho\alpha_{ij}^c$ and θ_{ij} densities for each EBSD maps with their original stepsize or re-sampled stepsize.

1000

Supplementary Figure S1: Compilation of the entrywise norm maps for all samples and the triplet θ_{13} , θ_{23} and θ_{33} maps for all sample.